Artificial Neural Network Analysis of Magnetohydrodynamic Flow and Thermal Radiation in Hybrid Nanofluid with Bio-Convection over a Stretching Sheet

Muhammad Akmal[1], Azhar Ali Zafar[1], Sohaib Abdal[2] and Nehad Ali Shah[3,*]

[1] Department of Mathematics, Government College University, Lahore, 54000, Pakistan

[2] Department of Mathematical Sciences, Saveetha School of Engineering, SIMATS, Chennai, 602 105, India

[3] Department of Mechanical Engineering, Sejong University, Seoul, 05006, Republic of Korea

Revista Internacional
Métodos numéricos
para cálculo y diseño en ingeniería
RIMNI
UNIVERSITAT POLITÈCNICA DE CATALUNYA BARCELONATECH
In cooperation with CIMNE

INFORMATION

Keywords:
Hybrid nano-fluid
magneto-hydrodynamics
bio-convection
thermal radiation
artificial neural network

DOI: 10.23967/j.rimni.2025.10.72451

SCIPEDIA Revista Internacional de Métodos Numéricos para Cálculo y Diseño en Ingeniería

Revista Internacional Métodos numéricos para cálculo y diseño en ingeniería RIMNI

In cooperation with CIMNE

Artificial Neural Network Analysis of Magnetohydrodynamic Flow and Thermal Radiation in Hybrid Nanofluid with Bio-Convection over a Stretching Sheet

Muhammad Akmal[1], **Azhar Ali Zafar**[1], **Sohaib Abdal**[2] **and Nehad Ali Shah**[3,*]

[1]Department of Mathematics, Government College University, Lahore, 54000, Pakistan

[2]Department of Mathematical Sciences, Saveetha School of Engineering, SIMATS, Chennai, 602 105, India

[3]Department of Mechanical Engineering, Sejong University, Seoul, 05006, Republic of Korea

ABSTRACT

This study investigates the flow and heat transfer of a hybrid nanofluid including alumina and titanium dioxide nanoparticles across a stretched sheet in the presence of a magnetic field, thermal radiation, and bio-convection. The problem is significant because hybrid nanofluids are increasingly employed in industrial cooling, biomedical transport, and energy systems that need accurate prediction of nonlinear thermal and solutal behavior. The governing nonlinear equations were transformed into ordinary differential form and computationally solved via a fourth-order Runge-Kutta method. In addition to this, an artificial neural network model was created to reproduce the numerical results and evaluate prediction abilities. The results show that stronger magnetic forces reduce velocity by about 18%, while higher radiation levels increase fluid temperature by nearly 22%. Increasing the Lewis number lowers nanoparticle concentration by roughly 15%, and higher bioconvection effects reduce microorganism density by about 12%. The neural network achieved excellent agreement with the numerical results, with regression values close to 1 and a mean squared error of order 10^{-10}. The findings indicate that hybrid nano-fluids offer enhanced heat transfer and flow stability under MHD conditions, supporting potential improvements in fluid and thermal performance for applications requiring precise thermal management.

OPEN ACCESS

Received: 27/08/2025

Accepted: 05/11/2025

Published: 16/04/2026

DOI
10.23967/j.rimni.2025.10.72451

Keywords:
Hybrid nano-fluid
magneto-hydrodynamics
bio-convection
thermal radiation
artificial neural network

Nomenclature

B_o	Magnetic field parameter (T)
ϕ	Non-dimensional concentration
c_p	Specific heat at constant pressure (J/kgK)
C_w	Hybrid nano-fluid concentration beside the sheet
C_∞	Concentration of nano-fluid distant from the sheet
D_B	Brownian diffusion coefficient (m^2/s)

*Correspondance: Nehad Ali Shah (nehadali199@sejong.ac.kr).

D_T	Thermo-phoretic diffusion coefficient $\left(\mathrm{m}^2/\mathrm{s}\right)$
E_c	Coefficient of viscous dissipation (Pa·s)
κ	Thermal conductivity coefficient (W/m·K)
Lb	Lewis number for microorganisms
R	Radiation parameter
Le	Lewis number for concentration
T	Temperature symbolization (K (°C))
T_∞	Temperature away from the stretching sheet (K (°C))
T_w	The temperature on the stretching sheet (K (°C))
u, v	Velocity components aligned with the x-axis and y-axis (m)
ϑ_f	Kinematic viscosity $\left(\mathrm{m}^2/\mathrm{s}\right)$
H_a	Magnetic field parameter
$(\rho Cp)_{hnf}$	Heat capacity of hybrid nanofluid (J/kgK)
h_1	Thermal convective coefficient $\left(\mathrm{W}/\left(\mathrm{m}^2\mathrm{K}\right)\right)$
θ	Non-dimensional temperature
Nu_x	Nusselt number
h_2	Concentration convective coefficient (m/s)
μ_{hnf}	Dynamic viscosity of hybrid nano-fluid (Pa·s)
ρ_{hnf}	Hybrid nano-fluid density $\left(\mathrm{Kg}/\mathrm{m}^3\right)$
Cf_x	Drag force coefficient
δ_1	Viscosity parameter (Pa·s)
δ_2	Parameter of thermal conductivity (W/(m·K))
f	Stream function normalized by non-dimensional quantities
λ	Parameter of slip velocity (m/s)
f_w	Suction/injection velocity (m/s)
u_w	The velocity related to the stretching motion (m/s)
P_r	Prandtl Number
q_r	Radiant heat flow (W)
λ_1	Slip velocity coefficient
k_{hnf}	Thermal conductivity of hybrid nanofluid $\left(\mathrm{m}^2/\mathrm{s}\right)$
Y_t	Thermophoresis parameter
Y_b	Brownian motion parameter $\left(\mathrm{m}^2/\mathrm{s}\right)$

1 Introduction

Fluid flow and heat transmission across stretched sheets are critical in many industrial processes, including polymer extrusion, fiber coating, food processing, and biomedical applications. Nanofluids, which are base fluids encapsulated in nanoparticles, have grown in popularity over the last two decades due to their potential to improve thermal conductivity and energy transmission. Hybrid nanofluids made up of several nanoparticles have recently been created to outperform standard nanofluids in terms of temperature and flow. These improved fluids have opened up new possibilities for heat control, energy conversion, and unique industrial applications. External impacts such as magnetic fields, thermal radiation, and bio-convection have also piqued researchers' attention, as these mechanisms play critical roles in the velocity, temperature, and concentration profiles of nanofluidic systems. Magnetic fields impose Lorentz effects on flow, altering thermal profiles. At high temperatures, radiation predominate, and bio-convection is caused by the bulk motion of motile microorganisms, which affects mass transport and stability. Simultaneously, artificial intelligence

technologies, notably artificial neural networks (ANNs), are increasingly being used to simulate nonlinear transport processes and offer predictive capabilities at a low computing cost.

Fluid flow over stretched sheets is of interest because they have numerous industrial uses. Manufacturing operations include fiber and wire coating, polymer extrusion, melting, food processing, spinning, and mechanical molding, among others. A nano-fluid is the suspension of tiny particles (size of the particles is $\leq$100 nm) in a pure fluid. The base (pure) fluids are oil, water, or ethylene glycol, etc. Nanoparticles include silver (Ag), alumina (Al_2O_3), (Cu) copper, and (CuO) copper oxide. These fluids enhance thermal conductivity and heat transfer of base (pure) fluids. Brownian motion and thermo-phoresies are applied in the Williamson nano-fluid flow over an expanding sheet, which was examined by Nayak et al. [1]. The impact of the morphology of nanoparticles in Al_2O_3 water and Cu water-based nano-fluids on a nonlinear stretching sheet with thermal radiation was examined by Gireesha et al. [2]. The non-Newtonian nano-fluid (NNNF) flows across a permeable Riga surface caused by the concentration of pollutant discharge (PDC) across the thermal radiation flow, and two different varieties of NNNF were studied by Jubair et al. [3]. The impact of activation energy, thermal radiation, magnetic fields, external sources of heat, and slip conditions on the bio-convective Casson nano-fluid flow was discussed by Galal et al. [4]. The Carreau nano-fluid flow on an unsteady extending cylindrical sheet with thermal radiation, non-Darcy porous medium, viscous dissipation, and Joule heating was studied by Gorfie et al. [5].

Hybrid nano-fluids are heat transfer fluids that incorporate tiny particles (less than 100 nm). These fluids combine two or three solid components and base fluids (water, ethylene glycol, or a water-ethylene glycol combination, motor oil, kerosene, vegetable oil, and paraffin oil). Nonetheless, a hybrid nano-fluid was developed to improve the thermal properties of a standard nano-fluid. A hybrid nano-fluid is an enhanced fluid that contains two or more tiny particles, which have the potential to increase the heat transfer rate due to symbiotic effects. In addition, the needed heat transmission can be achieved by mixing the appropriate nanoparticles. Entropy generation and flow behavior are comprehensively described for a mixed convective ($MgO\text{-}ZnO/H_2O$) hybrid nano-fluid over an exponentially stretching sheet with the Tiwari-Das model, but it considers the effects of thermal radiation, Joule heat, viscous dissipation, velocity slip, thermal slip, and varying thermal conductivity at the boundary and is compared with already published results and shows an excellent coincidence, which proves the validity and reliability of the offered model that was studied by Kandukoori et al. [6]. Waseem et al. [7] discussed a study on heat and mass transfer in a hybrid Sisko nano-fluid. Gul et al. [8] studied the Brownian and thermo-phoretic parameters of 3D MHD hybrid nano-fluid flow over a bi-directionally stretching sheet. Alharbi et al. [9] utilized hybrid nano-fluid flow with the Tiwari-Das model and COMSOL Multiphysics 6.0 close to the stretching/shrinking sheet stagnation point. Hybrid nanofluid flow, based on the dispersal of aluminum oxide (Al_2O) and copper (Cu) nanoparticles in ethylene glycol, with a linearly stretching sheet inclined $\zeta = \pi/6$ in a porous medium. The Lorentz force, solar radiation, heat generation, chemical reactions, and plate permeability are considered in the model because the cylindrical nanoparticles are taken from the view of their excellent thermal characteristics, which were studied by Jeelani et al. [10]. Using a stretching sheet with porous material and a heat source/sink and exploring the magneto-radiative flow properties of a hybrid nanofluid are contentious topics that examine the effects of convective heat transmission, thermal radiation, heat absorption, and MHD by Radhika et al. [11].

The macroscopic dynamics of electrically conducting fluids are described by the single fluid model known as magneto-hydrodynamics (MHD). Managing toxic waste and refining crude oil more efficiently can be achieved by the petroleum industry with an understanding of MHD nano fluid flow. Studying magneto-hydrodynamic (MHD) heat and mass transport in nano-fluid flow over

two-dimensional boundary layers in porous media has significant applications in many sectors. The radiative couple-stress magneto-hydrodynamic (MHD) nano-fluid flow generation in a permeable vertical wall channel with a time-fractional order framework. Those of thermal radiation, thermo-phoresis, Brownian motion, suction/injection, viscous dissipation, Joule heating, buoyancy forces, couple-stress heating, and an applied magnetic field are included. The findings provide useful information on thermodynamic irreversibility, and the optimization of heat transfer in a nano-fluid-based system was studied by Khan et al. [12]. The role of viscous dissipation on constant heat transfer in chemically reactive MHD nanofluid flow in a vertical cone with porous medium was discussed by Sademaki et al. [13]. In this study, thermo-phoresis and Brownian motion affect the nanofluid motion, which indicates that the heat transfer decreases due to radiation and Brownian motion and rises due to the internal heat source and thermo-phoresis. The second order slips flow of MHD nanofluids through a thin needle with dynamically varying temperature characteristics was investigated by Bilal et al. [14]. Besides viscosity and thermal conductivity in a temperature-dependent manner under a zero-mass flux condition, the effects of thermophoretic and Brownian motion are also considered in the analysis. The findings indicate that the rate of heat transfer is increased by a rise in the surface thickness of the needles, whereas a rise in the viscosity of the fluid leads to a drop in the temperature of the fluid. Lutera et al. [15] discussed the influences of heat radiation on the electrically conducting nanofluid flow by natural convection and the transversely accelerating surface flow of water-based nanofluid past the surface. The effect of internal heat production and radiation on thermal and momentum boundary layers is analyzed. The results indicate that thermal radiation increases velocity and temperature, which is beneficial in the case of solar collectors. The Darcy-Forchheimer MHD flows through the uneven elastico-viscous sheet of different thicknesses, inclusive of heat sources, chemical processes, coupled Soret-Dufour effects, was discussed by Mittal et al. [16]. It is also observed that the flow is dependent on the sheet stretching, the magnetic field, inertia, permeability, volume fraction of nanoparticles, and viscosity. Hafeez et al. [17] investigated the twofold solutions of hybrid nanofluid flow over a shrinking/stretching wedge that are influenced by melting heat, surface slip conditions, heat source/sink, and thermal radiation. The results have shown that radiation intensity increases heat transfer, but higher melting temperature decreases the Nusselt number. The three-dimensional Casson nanofluid flow over a long porous surface was studied under the Navier-Stokes paradigm, whereby calculations were done in MATLAB by a new three-stage Lobatto IIIA hybrid. There is a lot of information on how the governing parameters can control the flow behavior of Casson nanofluids, which is important in many engineering practices. It was noted that as the magnetic parameter rises, there is an induction of a Lorentz force that suppresses the velocity field and boosts the temperature distribution, which was discussed by Boudjemline et al. [18]. Concurrent features of the entropy formation in a square cavity with a circular item in the middle and four fins attached diagonally at each corner, as well as the natural convection flow of heat and mass transfer. A non-Newtonian fluid is poured into the enclosure, and an inclining magnetic field is applied, as discussed by Ahmad et al. [19].

Thermal radiation, the process of energy transfer through electromagnetic waves, further complicates the study of fluid dynamics. Comprehending the relationship between thermal radiation and fluid flow becomes essential in high-temperature situations or systems where radiation affects heat transfer. Since nanoparticles can alter the fluid's radiative characteristics, this is especially crucial for nano-fluids and hybrid nano-fluids. Williamson hybrid Zn-SiO_2/H_2O nanofluid flow and heat transfer dynamics across a porous surface under the effects of activation energy, thermal radiation, and motile microorganisms were studied by Farooq et al. [20]. The findings indicate that an increase in the magnetic field parameter will inhibit the speed of the fluid, but the rotational parameter will

boost the concentration of motile microorganisms. Madhukesh et al. [21] discussed the chemical reaction and thermal transport analysis in ternary hybrid nanofluid flow across a vertical cylinder. The results demonstrate that to increase the chemical reaction parameter, radiation will lower the heat profile, mixed convection, and melting, and critical shear stress will increase the velocity, and the concentration profile. Analysis of irreversibility in tetra-hybrid non-Newtonian fluids with Soret-Dufour effects and thermal radiation over porous inclined stretching sheets. Optimization of entropy generation is achieved by increasing the magnetic parameter, and a decrease in the coefficient of skin friction in tangent hyperbolic hybrid nanofluid is caused by velocity slip. The maximum heat transfer rate is observed in Casson tetra-hybrid nanofluid, which increases by 52 percent as the Soret number increases, as discussed by Amudhini et al. [22]. The temperature field is caused by the flow of fluids in a thin film, specifically the energy transfer in a dissipative liquid by way of radiation. The results show that, when thermal radiation is added, it reduces the temperature of the thin film, and an increase in the thermal diffusion will result in a further reduction of the temperature at the constant parameter conditions. Also, the findings depict the effect of the change in Reynolds number on the behavior of the heat and mass transfer in the model, which was discussed by Mustafa et al. [23]. The Phan-Thien-Tanner fluid model under peristaltically flowing conditions with a permeable porous wall, effects of heat transmission and thermal radiation. The findings indicate that fluid elasticity increases with the Weissenberg number, which promotes energy storage and redistribution in the process of deformation. In addition, an increase in parameters (Darcy, Prandtl, and radiation) will decrease the temperature profile, which indicates that permeability and radiation are important in governing the effectiveness of flow and heat transfer, which was discussed by Channakote et al. [24].

The creation of structures due to a swimming microbe's motion is the focus of the study of bio-convection. Densities fluctuate because a thick layer of gyrotronic bacteria frequently forms on the liquid's upper half. A stream arises above and below as the microbe descends when the thick layer separates. The scientific word for this phenomenon is bioconvection. These days, a variety of harmful disorders are being identified using biotechnology and nano-fluids. Three-dimensional theoretical analysis of hybrid nanofluid flow of gyrotactic microorganisms in an induced magnetic field. The study focuses on how different parameters related to flow affect temperature, velocity, distribution of nanoparticles, and density of microorganisms. Findings show a strong adjustment of these physical quantities, which indicates a close interdependence between magnetic induction and microorganism motility. The results lead to a better insight into the description of transport in bioconvective hybrid bio-nanofluids, which was discussed by Mabrouk et al. [25]. Magneto-hydrodynamic fluid flow of Reiner-Rivlin nanofluid over a stretchable, porous sheet under gyrotactic microorganisms. The model uses dissipative forces, Joule heating, radiative heat flux, Brownian motion, thermophoresis, and chemical reaction with altered Arrhenius kinetics. Findings indicate that the fluid velocity reduces as the Hartmann number and porosity parameter increases, which influences the momentum transport. The article gives an insight into the heat and mass transfer control of electrically conducting nanofluid systems, which was discussed by Haq et al. [26]. Dynamically stretched micropolar nanofluids flow in a gyrotactic microorganism-containing Darcy-Forchheimer porous medium with the inclusion of the Cattaneo-Christov heat flux with radiation and heat source effects and Buongiorno models. It has been found that the magnetic field increases the microrotation profile, but a greater micropolar parameter inhibits it. The porosity, radiations, Brownian movement, and thermophoresis are the increasing factors of the thermal distribution, whereas increased thermal relaxation and temperature difference lead to the decreased thermal distribution, which was discussed by Reddy et al. [27]. The bioconvective movement of Casson micropolar nanofluid over a porous bidirectionally stretched surface. The

transport phenomena are studied using a non-Fourier heat conduction model that is the Cattaneo-Christov framework, which considers the radiation effects and chemical reactions. It has been observed that the porosity parameter and the micropolar fluid constantly improve the heat transfer, which was discussed by Hajlaoui et al. [28]. The magneto-bio-convective movement of a Maxwell nanofluid across a rotating disk surface, this analysis indicates that the thermal distribution is highly increased by the magnetic effects, Brownian motion, thermophoresis, heat sources, and thermal radiation. All these factors increase the rate of heat transfer, which proves to be very important in increasing thermal transport of bio-convective nanofluid systems, which was discussed by Algehyne et al. [29].

Artificial intelligence (AI) is a fast-growing sphere that tries to create systems that have the ability to imitate human-like reasoning, learning, and decision-making. Machine learning is one of the most important subfields of AI that allows computers to enhance their work with the help of experience without the need to be programmed. In this field, artificial neural networks (ANNs) are an effective computational model based on the structure and the working of the human brain. ANNs have been especially useful in pattern recognition, approximation of nonlinear functions, and the processing of complicated data. They are used in a very broad area of application, including robotics, autonomous systems, natural language processing, gaming, and medical diagnostics. The incredible success of ANNs has seen them become a key tool in solving difficult problems in the real world, which has resulted in innovation in science and technology. Artificial neural network (ANN) models were created to predict the generation of forming limit diagrams (FLDs) using tensile test outcomes of experimental data and literature on steel and aluminum sheet metals. The accuracy of ANN predictions was estimated after the training process with the help of the linear regression parameters and the absolute error analysis. In the case of steel sheet data, which was retrieved through the literature, the ANN predictions were further checked against the outcome of different empirical formulae. The results showed that there was a high correlation between the predicted and measured values, and this proved that ANN models made better approximations than the traditional linear and nonlinear models, which were studied by Czinege et al. [30]. It suggests a sequential approximate optimization algorithm with the combination of FEM, DDE, and ANN surrogate models. It is used for the optimal design of metal materials and the optimization of parameters of multi-stage metal forming processes. ANN surrogates are trained based on FEM-Python integration, and the generated data is through Latin hypercube sampling. Findings indicate that ANN models are more accurate and efficient than traditional models of response surfaces that utilize polygons, as discussed by Han et al. [31]. ANN-based method of maximizing entropy generation of micropolar tetra-hybrid nanofluids using a curved artery. The model takes into consideration the magnetic field effects, chemical reactions, viscous dissipation, Joule heating, and the external heating. The model is checked against published results, and the results are strongly consistent, which proves its reliability. Results have shown that the curvature radius increases micro-rotational velocity but decreases the Nusselt number, whereas radiation increases heat transfer, as discussed by Sharma et al. [32]. The application of artificial neural networks (ANNs) in heat transfer in thin layers investigates the behavior of Casson fluids by the effects of Hall current and Darcy-Forchheimer. The main aim is to predict the rate of heat transfer in non-Newtonian fluid flows with great accuracy, and in complex cases, it can be done using the conventional models, which are often not precise. The findings indicate that the ANNs yield very precise predictions of the Nusselt number, which is very close to training and theoretical data discussed by Ali et al. [33]. The heat radiation on the magneto-hydrodynamics (MHD) of *Cu* water-based Prandtl nanofluid flow through the artificial neural networks (ANNs). The nanoparticles are copper, which is added to improve thermal performance. The ANN model has a high degree of precision in predicting skin friction and Nusselt number profiles. Its outcomes are in great agreement with the data of numerical simulation,

proving the reliability of the model, as discussed by Shah et al. [34]. Artificial neural networks (ANNs) are used to study the heat transfer performance of a hybrid nanofluid (HNF) of water flow over a permeable stretching surface in the presence of an inclined magnetic field and thermal radiation. The Cattaneo-Christov heat flux model (CCHFM) is used to represent the nature of heat transfer in the boundary layer slip flow when the thermal conductivity varies, and the diffusion of nanoparticles is taken into account. Findings have shown that the magnetic parameter decreases the frictional drag coefficient, and the opposite is true when the nanoparticle volume fraction is increased, as discussed by Alimi et al. [35].

Combining a data-driven artificial neural network trained using the Levenberg–Marquardt method with a nonlinear magnetohydrodynamic–radiative hybrid nanofluid model with bio-convection essentially makes this study novel. This dual-framework method allows precise, affordable forecasting of velocity, temperature, concentration, and microorganism profiles in highly nonlinear flow regimes by quantitatively bridging the gap between intelligent prediction and numerical simulation. This combination of ANN learning and physics-based modeling offers a fresh approach to hybrid nanofluid and bio-thermal transport study.

Many such earlier research studies have contributed greatly; most of them have employed simplified models of nanofluids. These generally exclude very important nonlinear effects such as viscous dissipation, radiation-convection interaction, and bio-convection due to microorganism-induced activity. More importantly, most of these studies so far have considered single particle nanofluids, hence neglecting the synergistic effectiveness gained by hybrid nanoparticles. These simplifications limit the ability to explain the entire intricacy of thermal and solutal transport in actual engineering and biomedical systems.

The present study addresses these limitations by considering a nonlinear model of hybrid nanofluid flow along a stretching sheet under the conjugate influence of magnetohydrodynamics, thermal radiation, and bio-convection. This coupled model represents the field behavior of velocity, temperature, concentration, and motile microorganism fields and possesses a more realistic physical transport process representation. Furthermore, to complement numerical simulation results obtained based on the fourth-order Runge–Kutta method, the predictive analysis is carried out using an artificial neural network. This two-fold approach not only assures efficiency and dependability but also demonstrates an innovative way to pair state-of-the-art machine learning and nonlinear fluid dynamics, thereby transcending reduced models offered in earlier research.

2 Formulation of the Problem

In the present case, it is assumed that there is a hybrid nano-fluid, which is continuous, non-compressible, and flows in the region where the y-coordinate exceeds zero, from a permeable solid surface at, $y = 0$ with the reference point fixed at $x = 0$, as shown in Fig. 1a. The fundamental assumption is that the plate must sustain a constant temperature T_w across the sheet as well as the volume fraction of hybrid nano-fluid at the sheet's surface, represented by the symbol C_w. Additionally, a thin, solid surface that extends in the direction of the x-axis emerges from a slit at the beginning. The stretching speed, given by $u_w(x)$, is thought to change linearly from the initial value, with a positive constant value, represented by c. The hybrid nano-fluid's velocity vector U is thought to be made up of two basic portions, u, v which stand for the flow components in the x, y-directions, respectively. The study takes into account both when microorganisms move along the x-axis and y-axis with two-dimensional velocities u and v, bio-convection takes place, denoted by N_∞, at a significant distance from the sheet surface, volume fraction of the hybrid nanofluid and ambient fluid temperature,

denoted by C_∞, T_∞, respectively. Furthermore, the slip velocity phenomena affect the hybrid nano-fluid's motion, and in these particular circumstances, the constitutive equations governing the hybrid nano-fluid model are obtained in the subsequent form [36,37].

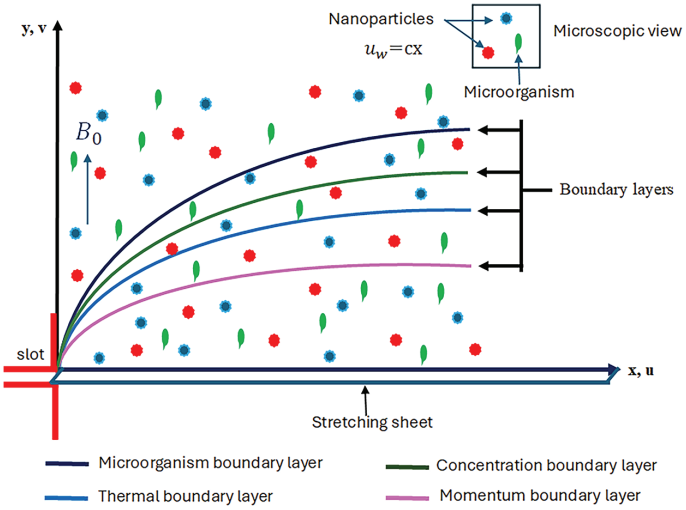

(a)

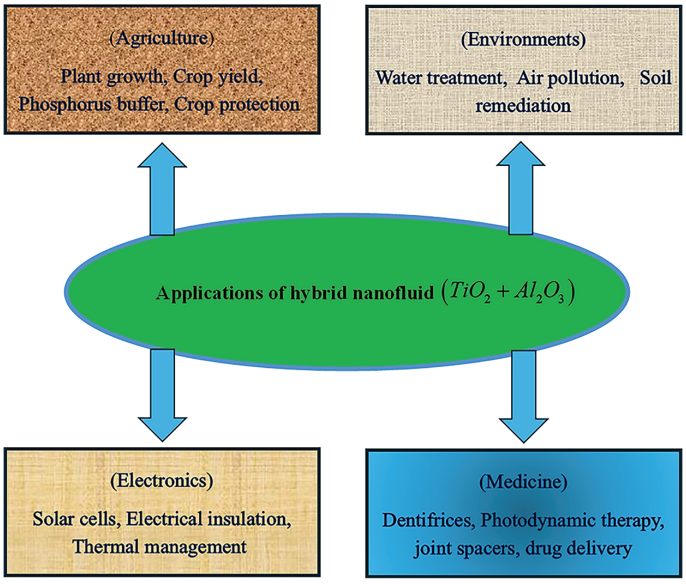

(b)

Figure 1: (a): Outline of the physical flow model showing hybrid nanofluid motion over a stretching sheet under the influence of magnetic field, radiation, and bio-convection; (b): Applications of hybrid nanofluids ($TiO_2 + Al_2O_3$ with water) across agriculture, environmental, electronic, and biomedical fields, highlighting their potential for improved heat transfer and flow stability

Fig. 1b demonstrates that due to their high thermal conductivity and heat transfer, $TiO_2 + Al_2O_3$/water-based hybrid nanofluids possess extensive applications in the fields of agriculture, medicine, and electronics. They can be used in agriculture to improve solar collectors, heating

greenhouses, irrigation, soil heating, and cooling of machinery, thus enhancing the use of energy and sustainable practices. They find application in the medical sector as they can be used to deliver drugs to specific regions, in photothermal therapy, cancer treatment, cooling biomedical devices, improving imaging, and sterilizing. They are used in electronics as very effective coolants in heat sinks, microchannel heat exchangers, and liquid coolants to CPUs, GPUs, and power devices, effectively preventing overheating, enhancing performance, and increasing the life of devices.

$$\nabla . U = 0 \tag{1}$$

$$U.\nabla u = \frac{1}{\rho_{hnf}} \frac{\partial}{\partial y}\left(\mu^*_{hnf} \frac{\partial u}{\partial y}\right) - \frac{\sigma_{hnf}}{\rho_{hnf}} \mathrm{B}_o^2 u + \frac{1}{\rho_{hnf}}\left[g^* \left(T - T_\infty\right) \rho_f \beta^* \left(1 - C_\infty\right) + g^* \left(\rho_p - \rho_f\right)\left(C_\infty - C\right) - \left(\rho_m - \rho_f\right)\left(N_\infty - N\right) g^* \gamma^*\right] \tag{2}$$

$$U.\nabla T = \frac{1}{\left(\rho c_p\right)_{hnf}} \frac{\partial}{\partial y}\left(K^*_{hnf} \frac{\partial T}{\partial y}\right) - \frac{\mu^*_{hnf}}{\left(\rho c_p\right)_{hnf}} \left(\frac{\partial u}{\partial y}\right)^2 + \tau\left[D_B \frac{\partial C}{\partial y}\frac{\partial T}{\partial y} + \frac{D_T}{T_\infty}\left(\frac{\partial T}{\partial y}\right)^2\right] - \frac{1}{\left(\rho c_p\right)_{hnf}} \frac{\partial q_r}{\partial y} \tag{3}$$

$$U.\nabla C = D_B\left(\frac{\partial^2 C}{\partial y^2}\right) + \frac{D_T}{T_\infty}\left(\frac{\partial^2 T}{\partial y^2}\right) \tag{4}$$

$$U.\nabla N = D_m\left(\frac{\partial^2 N}{\partial y^2}\right) + \frac{bw_c}{\left(C_\infty - C_w\right)} \frac{\partial}{\partial y}\left(N \frac{\partial C}{\partial y}\right) \tag{5}$$

here ρ represent the density of the fluid, σ the electrical conductivity, and μ the viscosity of the nanofluid. The behavior and characterization of the fluid in question are influenced by these characteristics taken together. In this regard, dynamics of the system under study are impacted by the use of a magnetic field, denoted by B_o, which acts perpendicular to the x-axis. The diffusion resulting from random particle motion is represented by the Brownian diffusion coefficient D_B, $\left(q_r = -\frac{4\sigma^*}{3k^*}\frac{\partial T^4}{\partial y}\right)$ which is the radiative heat flux and diffusivity of microorganisms D_m. Furthermore, the thermal diffusivity, denoted by α, controls the fluid temperature T, the density of motile microorganisms, N and C indicates the concentration of nanoparticles in the fluid, and the following set of requirements establishes the parameters in this case, outlining the limitations and relationships controlling the system being studied [36,37].

$$-D_B\left(\frac{\partial C}{\partial y}\right) = h_2\left(C_w - C\right), -K^*_{hnf}\left(\frac{\partial T}{\partial y}\right) = h_1\left(T_w - T\right), \; at \; y = 0 \tag{6}$$

$$u = cx + \frac{\lambda_1}{\mu_{hnf}}\left(\mu^*_{hnf}\frac{\partial u}{\partial y}\right), \mathrm{v} = -\mathrm{v}_w, \text{at y} = 0, \mathrm{u} \to 0, \mathrm{T} \to \mathrm{T}_\infty, \mathrm{C} \to \mathrm{C}_\infty, \mathrm{N} \to \mathrm{N}_\infty \text{ asy} \to \infty \tag{7}$$

Certain normalized variables are incorporated into the created equations to convert them into a dimensionless form. The similarity transformed and varying thermal conditions [36,37].

$$u = \frac{\partial \psi}{\partial y}, v = -\frac{\partial \psi}{\partial x}, \psi = \sqrt{c\vartheta_f} x f\left(\eta\right), \eta = \sqrt{\frac{c}{\vartheta_f}} y, \phi\left(\eta\right) = \frac{C - C_\infty}{C_w - C_\infty}, \theta\left(\eta\right) = \frac{T - T_\infty}{T_w - T_\infty},$$

$$\chi\left(\eta\right) = \frac{N - N_\infty}{N_w - N_\infty} \tag{8}$$

$$\mu^*_{hnf} = \mu_{hnf}\left(e^{-\delta_1 \theta}\right), \mathrm{K}^*_{hnf} = K_{hnf}\left(1 + \delta_2 \theta\right) \tag{9}$$

Physical parameters of interest, like local Nusselt number (Nu_x) and local skin-friction coefficient (Cf_x), are defined as [36]:

$\mathrm{Re}_x^{1/2} Cf_x = -f''(0)\, e^{-\delta_1 \theta}(0)$, $\mathrm{Nu}_x \mathrm{Re}_x^{-1/2} = -\theta'(0)$, $\mathrm{Re}_x = \frac{u_w(x)x}{\vartheta_{hnf}}$. Here $u_w(x)$ is the stretching velocity (e.g., $u_w(x) = cx$ for a linearly stretching sheet). The governing Eqs. (2)–(5) can be stated dimensionless as follows using the variables listed in Eqs. (8) and (9):

$$\frac{A_1}{A_3}\left[\frac{d^3f}{d\eta^3} - \delta_1 \frac{d^2f}{d\eta^2}\frac{d\theta}{d\eta}\right] e^{-\delta_1\theta} + f\frac{d^2f}{d\eta^2} - \frac{A_2}{A_3} H_a \frac{df}{d\eta} - \left(\frac{df}{d\eta}\right)^2 + \frac{1}{A_3}(\theta - N_r\phi - N_c\chi)\lambda = 0 \tag{10}$$

$$\frac{A_4}{A_5 P_r}\left[\left(1 + \frac{R}{A_4} + \delta_2\theta\right)\frac{d^2\theta}{d\eta^2} + \delta_2\left(\frac{d\theta}{d\eta}\right)^2\right] + f\frac{d\theta}{d\eta} + Y_b\left(\frac{d\theta}{d\eta}\frac{d\phi}{d\eta}\right) + Y_t\left(\frac{d\theta}{d\eta}\right)^2 - \frac{A_1}{A_5} E_c e^{-\delta_1\theta}\left(\frac{d^2f}{d\eta^2}\right)^2 = 0 \tag{11}$$

$$\frac{d^2\phi}{d\eta^2} + Lef\frac{d\phi}{d\eta} + \left(\frac{Y_t}{Y_b}\right)\frac{d^2\theta}{d\eta^2} = 0 \tag{12}$$

$$\frac{d^2\chi}{d\eta^2} + Lbf\frac{d\chi}{d\eta} - P_e\left[(\chi + \varpi)\frac{d^2\phi}{d\eta^2} + \frac{d\phi}{d\eta}\frac{d\chi}{d\eta}\right] = 0 \tag{13}$$

The boundary conditions are represented as

$$\begin{gathered} f(0) = f_w, f'(0) = 1 + \lambda e^{-\delta_1\theta(0)} f''(0), \theta'(0) = -\mathrm{B}i_1\left(\tfrac{1-\theta(0)}{1+R+\delta_2(0)}\right), \phi'(0) = -\mathrm{B}i_2(1-\phi(0)), \\ f'(\infty) \to 0, \phi(\infty) \to 0, \theta(\infty) \to 0, \chi(\infty) \to 0 \end{gathered} \tag{14}$$

where, Magnetic field parameter $\left(H_a = \frac{\sigma_f \mathrm{B}_o^2}{(c_p)_f}\right)$, The Prandtl number $\left(P_r = \frac{\vartheta_f (\rho c_p)_f}{k_f}\right)$, Brownian motion parameter $\left(Y_b = \frac{\tau D_B (C_w - C_\infty)}{\vartheta_f}\right)$, Thermophoresis parameter $\left(Y_t = \frac{\tau D_T (T_w - T_\infty)}{\vartheta_f T_\infty}\right)$, Thermal Biot number $\left(\mathrm{B}i_1 = \left(\frac{h_1}{k}\right)\sqrt{\frac{\vartheta_f}{c}}\right)$, Concentration Biot number $\left(\mathrm{B}i_2 = \left(\frac{h_2}{D_B}\right)\sqrt{\frac{\vartheta_f}{c}}\right)$, Eckert number $\left(E_c = \frac{u_w^2}{(cp)_f (T_w - T_\infty)}\right)$, Radiation parameter $\left(R = \frac{16\sigma_f T_\infty^3}{3k^* k_f}\right)$, Lewis number $\left(Lb = \frac{\vartheta_f}{D_m}\right)$, biological convection Lewis number $\left(Le = \frac{\vartheta_f}{D_B}\right)$, Peclet number $\left(P_e = \frac{bw_c}{Dm}\right)$, density ratio of motile microorganism $\left(\varpi = \frac{N_\infty}{N_w - N_\infty}\right)$, mixed convection parameter $\left(\lambda = \frac{\beta^* g^* (1 - C_\infty)(T_w - T_\infty)}{c^2 x}\right)$, buoyancy ratio parameter $\left(N_r = \frac{(\rho_p - \rho_f)(C_w - C_\infty)}{\rho_f \beta^* (1 - C_\infty)(T_w - T_\infty)}\right)$, Rayleigh number of bio-convection $\left(N_c = \frac{(\rho_m - \rho_f)(N_\infty - N_w)\gamma^*}{\rho_f \beta^* (C_\infty - 1)(T_w - T_\infty)}\right)$, and $\left(A_1 = \frac{\mu_{hnf}}{\mu_f}\right)\left(A_2 = \frac{\sigma_{hnf}}{\sigma_f}\right)$, $\left(A_3 = \frac{\rho_{hnf}}{\rho_f}\right)\left(A_4 = \frac{k_{hnf}}{k_f}\right)$, $\left(A_5 = \frac{(\rho c_p)_{hnf}}{(\rho c_p)_f}\right)$ are ratios between hybrid nanofluids and base fluid's dynamics viscosities, electric conductivities, densities, thermal conductivities, and heat capacities.

In the current study, constant thermophysical properties were used as given in Tables 1 and 2. Since the present work aims to analyze the combined nonlinear effects of MHD, radiation, and bio-convection in hybrid nanofluids, using constant properties keeps the problem manageable without affecting universal trends of velocity, temperature, concentration, and microorganism profiles.

Table 1: Thermophysical properties of the hybrid nanofluid used in this study. Properties include viscosity, density, specific heat, thermal conductivity, and electrical conductivity

Properties	Hybrid nano-fluid
Dynamic viscosity	$\mu_{hnf} = \frac{\mu_f}{(1-\varphi_1)^{2.5}(1-\varphi_2)^{2.5}}$
Density	$\rho_{hnf} = (1-\varphi_2)\left[(1-\varphi_1)\rho_f + \varphi_1\rho_{s_1}\right] + \varphi_2\rho_{s_2}$
Heat capacity	$(\rho c_p)_{hnf} = [(1-\varphi_1)(\rho c_p)_f + \varphi_1(\rho c_p)_{s_1}](1-\varphi_2) + \varphi_2(\rho c_p)_{s_2}$
Thermal conductivity	$k_{hnf} = k_{nf}\left[\frac{(s-1)k_{nf} + k_{s_2} - (s-1)\varphi_2(k_{nf} - k_{s_2})}{(s-1)k_{nf} + k_{s_2} + \varphi_2(k_{nf} - k_{s_2})}\right]$
Electrical conductivity	$\sigma_{hnf} = \sigma_{nf}\left[\frac{\sigma_{s_2} + (s-1)\sigma_{nf} - (s-1)\varphi_2(\sigma_{nf} - \sigma_{s_2})}{\sigma_{s_2} + (s-1)\sigma_{nf} + \varphi_2(\sigma_{nf} - \sigma_{s_2})}\right]$

Table 2: Basic properties of nanoparticles (Al_2O_3 and TiO_2) and the base fluid (water), taken from the literature for hybrid nanofluid formulation

Properties	Al_2O_3 (Alumina)	TiO_2 (Titanium Dioxide)	Base fluid (Water)
$\rho\ (kg/m^3)$	3970	4250	997.0
C_p (J/kgK)	765	686.2	4180
k (W/mK)	40	8.9538	0.6071

3 Numerical Scheme

Eqs. (10)–(13) with boundary conditions Eq. (14), MATLAB software is used to numerically solve equations using the Runge-Kutta method of order four. The fourth-order Runge-Kutta technique is a MATLAB numerical algorithm for resolving ordinary differential equation boundary value problems (BVPs). Let's now define the new variable in Eq. (15).

$$y_1 = f, y_2 = f', y_3 = f'', dy_3 = f''', y_4 = \theta, y_5 = \theta', dy_5 = \theta'', y_6 = \phi, y_7 = \phi', dy_7 = \phi'', \\ y_8 = \chi, y_9 = \chi', dy_9 = \chi'' \tag{15}$$

The four connected higher-order differential equations, (10)–(13), can be expressed as follows using Eq. (15).

$$dy_3 = \frac{A_3}{A_1 e^{-\delta_1\theta}}\left[\frac{A_1}{A_3}(\delta_1 y_3 y_5)\, e^{-\delta_1\theta} - y_1 y_3 + \frac{A_2}{A_3}H_a y_2 + (y_2)^2 - \frac{1}{A_3}(y_4 - N_r y_6 - N_c y_8)\,\lambda\right]$$

$$dy_5 = \frac{A_5 P_r}{(A_4 + R + A_4\delta_2 y_4)}\left[-\frac{A_4}{A_5 P_r}\delta_2 (y_5)^2 - y_1 y_5 - Y_b (y_5 y_7) - Y_t (y_5)^2 + \frac{A_1}{A_5}E_c e^{-\delta_1\theta}(y_3)^2\right]$$

$$dy_7 = -Ley_1 y_7 - \left(\frac{Y_t}{Y_b}\right) dy_5$$

$$dy_9 = -Lby_1 y_9 + P_e\left[(y_8 + \varpi)\, dy_7 + y_7 y_9\right].$$

These altered equations were solved using the traditional fourth-order Runge–Kutta (RK4) technique using a shooting method on the MATLAB platform. A step of $\Delta\eta = 0.001$ was used, and convergence occurred when successive iterations differed by less than 10^{-6}. A far-field boundary was at $\eta\infty = 10$, well justified by sensitivity tests. Grid refinement showed changes below 0.1%, ensuring stability and accuracy of results.

Neural Network Modeling Approach

A supervised feed-forward backpropagation neural network was used to predict and simulate the output of the nonlinear hybrid nanofluid flow model. The training dataset was created from the numerical solutions that were obtained using the fourth-order Runge–Kutta (RK4) method. To ensure successful training and generalization, the dataset was divided into 70% for training, 15% for validation, and 15% for testing.

The architecture employed in the network was ten hidden layers, one output layer, and an input layer. The hidden layers were all built with a nonlinear transfer capability using the 'tansig' activation function, which is best at picking out complex nonlinear relationships. The output layer used the 'purelin' activation function to produce continuous numerical outputs. The network was trained using the Levenberg–Marquardt (LM) optimization algorithm, which was chosen for its stability and fast convergence when tackling nonlinear problems.

Convergence was tracked during training with the mean squared error (MSE) as the performance metric. Training stopped automatically if the validation error failed to decrease for six epochs in a row, preventing overfitting and guaranteeing the generalization capability of the model. The values of the regression close to 1 and extremely low MSE indicated that the network was correctly reproducing the numerical values and could be used as a good prediction tool.

Levenberg–Marquardt Supervised (LMS) Methodology.

The ANN was trained using the Levenberg–Marquardt Supervised (LMS) learning algorithm. LMS is a second-order optimization technique that combines the stability of gradient descent and the efficiency of the Gauss–Newton method. LMS attempts to reduce the mean squared error (MSE) between ANN predictions and numerical RK4 solutions. The method was employed because it provides rapid convergence and excellent performance in handling nonlinear datasets such as hybrid nanofluid transport models.

4 Results and Discussion

In this section, the numerical and neural network results of the bio-convective hybrid nanofluid flow in the presence of a stretching sheet under the influence of a magnetic field and motile microorganisms are compared and discussed. The effects of the physical parameters on the velocity, temperature, concentration, and profile of microbe distribution are well explored. The effectiveness and accuracy of the proposed model approach are also estimated with the help of comparative studies involving the numerical solutions and the predictions of artificial neural networks. The findings indicate that the developed model can be useful and provide significant physical inputs.

4.1 Hybrid Nanofluid (HNF) Model Discussion

Fig. 2 gives a detailed discussion in order to depict the effects of different parameters, such as the magnetic field parameter H_a, radiation parameter R, Lewis number of concentration Le, and Lewis number of the motile microorganisms Lb, on the variables of $f'(\eta)$, $\theta(\eta)$, $\phi(\eta)$, and bio-convection $\chi(\eta)$. Fig. 2a demonstrates that the velocity profile $f'(\eta)$ changed with different values of the magnetic

field parameter H_a. It is noted that the velocity profile reduces with increasing the magnetic field parameter, which can be explained by the effect of the Lorentz force as a resistive force that inhibits the movement of fluids. The Lorentz force, which is the force of the electromagnetic influence on a charged particle moving through an electric or magnetic field, is stronger when the magnetic fields are stronger, which in turn slows the fluid even further. In addition, the comparison of the nano-fluid and the hybrid nano-fluid shows that the hybrid nano-fluid has marginally better flow characteristics, suggesting that it is better in enhancing the thermal and momentum transport properties. Fig. 2b demonstrates that the temperature profile $\theta(\eta)$ changed with different values of the radiation parameter R. The fluid's temperature is significantly influenced by the thermal radiation parameter. An increase in the radiation parameter raises the fluid temperature by increasing the quantity of radiative heat transfer to the flow domain. This indicates that a high radiation parameter value will increase the temperature profile. This is because the system receives more energy from the stronger thermal radiation. Fig. 2c demonstrates that the concentration profile changed with the Lewis number Le. The Lewis number is a ratio of thermal diffusivity to mass diffusivity and is important to characterize species transport in the flow. A large value of the Lewis number, physiologically, implies that thermal diffusion prevails over mass diffusion, leading to a reduced speed of species diffusion. The resultant effect is that the increase in Lewis number Le causes the reduction of the concentration profile $\phi(\eta)$ and a thinning of the concentration boundary layer. This happens to be the case due to the decreased mass diffusivity, which limits the diffusion of species further away on the surface, so it decreases the overall concentration in the fluid field, and Fig. 2c also shows that the hybrid nano-fluid is better than the nano-fluid. Fig. 2d demonstrates that the concentration profile changed with different values of Lb. The profile of the microorganisms characterizes the concentration of the motile microorganisms in the fluid domain and depends on the bio-convection Lewis number Lb. Physically, a high bio-convection Lewis number means a reduced diffusivity of microorganisms compared with thermal diffusivity, which implies a reduced microorganism concentration layer and a reduction in the profile of microorganisms, and the figure also depicts that the hybrid nano-fluid is superior to the nano-fluid.

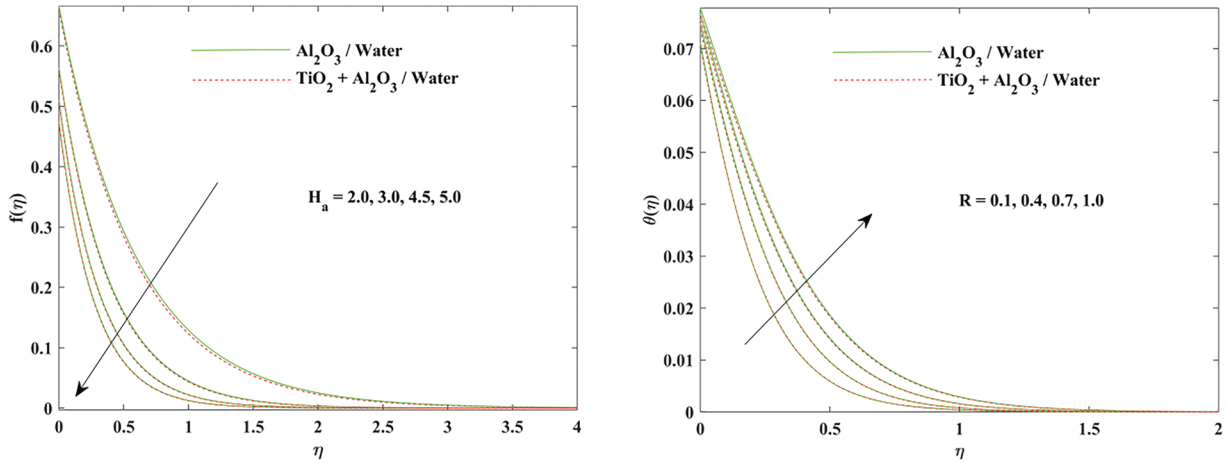

(a) Impact of H_a on $f'(\eta)$ **(b)** Impact of R on $\theta(\eta)$

Figure 2: (Continued)

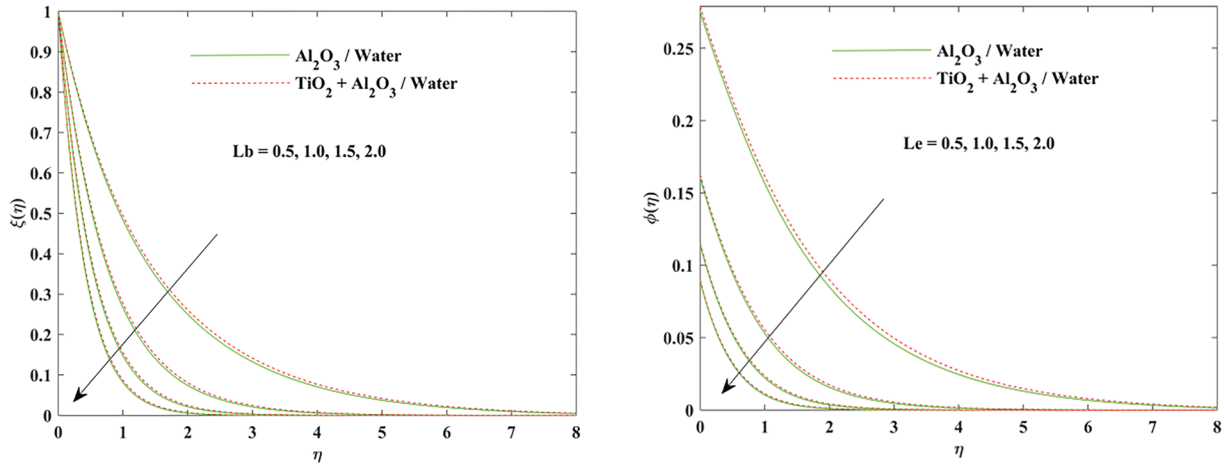

(c) Impact of Lb on $\chi(\eta)$ **(d)** Impact of Le on $\phi(\eta)$

Figure 2: (a–d): Effect of key parameters on physical profiles: (a) Magnetic parameter (H_a) on velocity; (b) Radiation parameter (R) on temperature; (c) Bioconvection Lewis number (Lb) on motile microorganism distribution; (d) Lewis number (Le) on nanoparticle concentration

4.2 Artificial Neural Network (ANN) Model Discussion

Using an artificial neural network algorithm for each output treated according to four scenarios made up of three distinct cases in Table 3 illustrates the changes in physical parameters H_a, R, Le, and Lb. Table 4 displays the LMS methodology results across various scenarios, as it demonstrates steady mean square errors (MSE) throughout the training, validation, and testing operations. The accuracy analysis and performance of the algorithm for all scenarios with three cases in the hybrid nano-fluid are achieved graphically in Figs. 3–9. The artificial neural network (ANN) demonstrates effective convergence through stable performance and minimal gradient values, as well as well-regulated mu. The proposed model demonstrates robust functionality because performance metrics remain high and MSE values stay low throughout the multiple testing scenarios. Fig. 3 shows the convergence nature of the training, validation, and testing of a neural network model in relation to the Mean Squared Error (MSE) metric. The horizontal line is the logarithmic scale of the number of epochs (trainings), and the vertical line is the MSE with the range of 10^{0} to 10^{-10}. Fig. 3a shows that during the training around epoch 0, the values of the MSE are large, which means that the initial approximation of the required output is poor. The MSE of all three datasets continues to decline at a very quick rate as the training advances, especially in the initial 20–30 epochs, which indicates that the model is effectively learning and adapting its parameters to reduce error. At this point, there is an increased, gradual decrease in error, which tends to lead to near-constancy as the model approaches convergence. 1.4071×10^{-10} the best validation performance is attained at epoch 142. Fig. 3b shows that during the training around epoch 0, the values of the MSE are large, which means that the initial approximation of the required output is not good. The MSE of all three datasets continues to decline at a very quick rate as the training advances, especially in some initial epochs, which indicates that the model is effectively learning and adapting its parameters to reduce error. At this point, there is an increased, gradual decrease in error, which tends to lead to near-constancy as the model approaches convergence. The best validation performance is 1.4591×10^{-10} attained at epoch 150. Fig. 3c shows that MSE is large at initial epochs and declines at a very quick rate, and gradually decreases. The best validation performance is 9.0862×10^{-11} attained at the epoch 151. Fig. 3d shows that the values of MSE are high at epoch 0,

which means the initial approximation of the required result is poor. The MSE continues to decrease with increasing the number of epochs and reaches the best performance 9.1245×10^{-11} at epoch 214.

Table 3: Four scenarios with three different cases each, showing selected physical parameters (magnetic field parameter, radiation parameter, Lewis number, and bioconvection Lewis number) considered in the analysis

Scenarios	Cases	Physical parameters			
		H_a	R	Le	Lb
Scenario 1	1	1.0			
	2	2.0			
	3	3.0			
Scenario 2	1		0.5		
	2		1.0		
	3		1.5		
Scenario 3	1			0.5	
	2			1.0	
	3			1.5	
Scenario 4	1				0.5
	2				1.0
	3				1.5

Table 4: Performance outcomes of the ANN using the Levenberg–Marquardt (LMS) algorithm for different scenarios and cases. Values include Mean Squared Error (MSE), performance, gradient, update parameter (μ), and epochs for training, validation, and testing phases

Scenario	Cases	MSE			Performance	Gradient	Mu	Epoch
		Training	Validation	Testing				
1.	1	9.10066e−11	1.15483e−10	6.68864e−10	1.1546e−10	9.954e−08	1e−09	191
	2	1.20165e−10	1.40712e−10	1.66978e−10	1.4071e−10	9.9869e−08	1e−09	142
	3	9.27523e−11	2.69205e−10	6.34823e−10	2.6921e−10	9.8054e−08	1e−09	121
2.	1	1.19166e−10	1.44548e−10	9.36411e−11	1.1548e−10	9.969e−08	1e−09	143
	2	1.11437e−10	1.45911e−10	8.33585e−11	1.4071e−10	9.8583e−08	1e−09	150
	3	1.07336e−10	9.57004e−10	1.45483e−10	9.57e−11	9.9929e−08	1e−09	154
3.	1	9.70246e−11	8.13147e−11	3.60587e−10	8.1315e−11	9.962e−08	1e−09	176
	2	1.12643e−10	9.8618e−11	1.31656e−10	9.0862e−11	9.8645e−08	1e−09	151
	3	9.90697e−11	1.18176e−10	7.09221e−10	1.1818e−10	9.8532e−08	1e−09	199
4.	1	1.04625e−10	3.48745e−10	1.06305e−10	3.4875e−10	9.962e−08	1e−09	163
	2	1.03599e−10	9.12447e−11	7.87653e−11	9.1245e−11	9.9708e−08	1e−09	214
	3	9.68156e−11	9.82607e−11	3.00265e−10	9.8261e−11	9.913e−08	1e−09	230

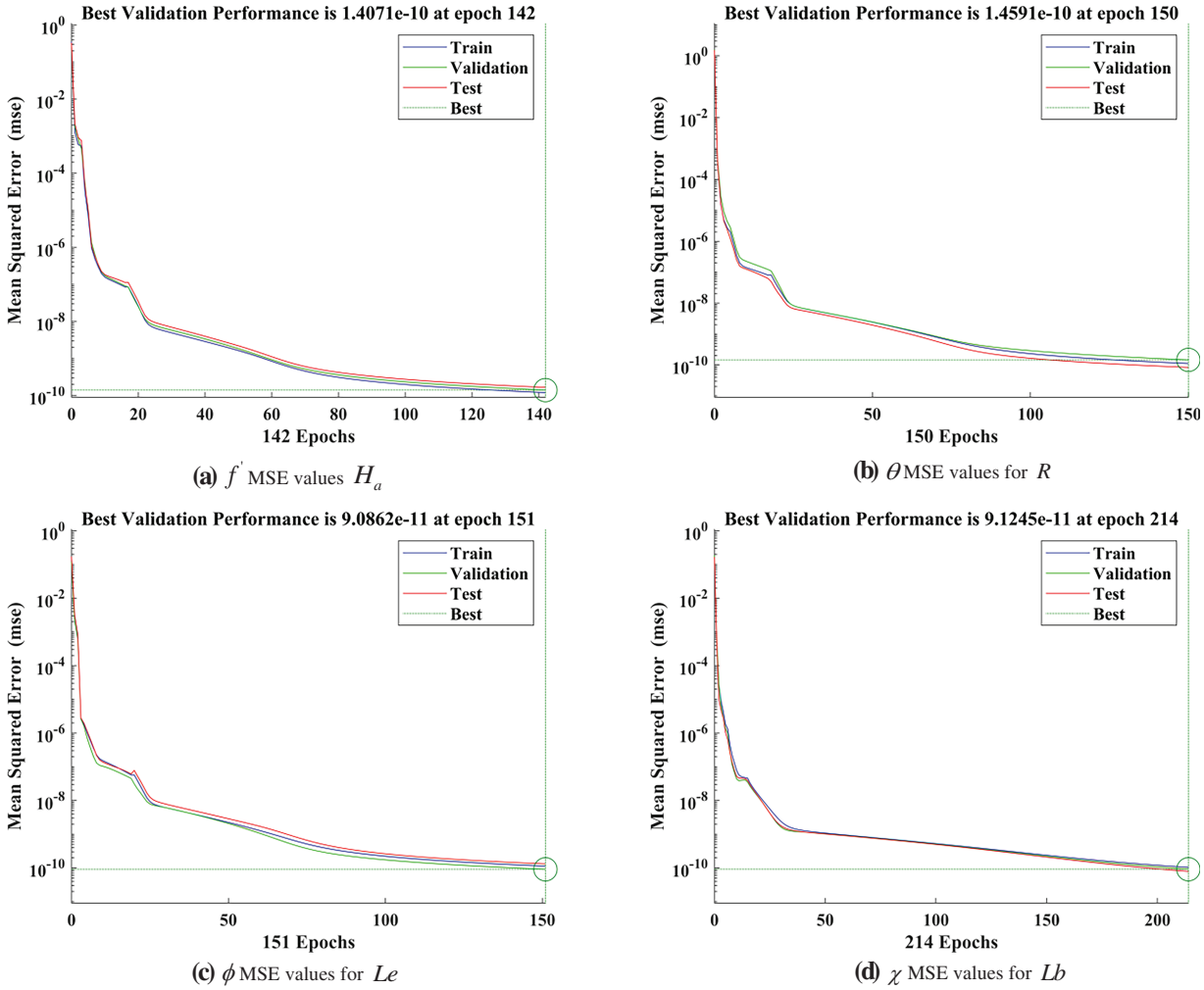

(a) $f^{'}$ MSE values H_a **(b)** θ MSE values for R

(c) ϕ MSE values for Le **(d)** χ MSE values for Lb

Figure 3: (a–d): Mean Squared Error (MSE) variation with epochs for all four scenarios of hybrid nanofluid flow, illustrating convergence behavior of the ANN model during training, validation, and testing phases

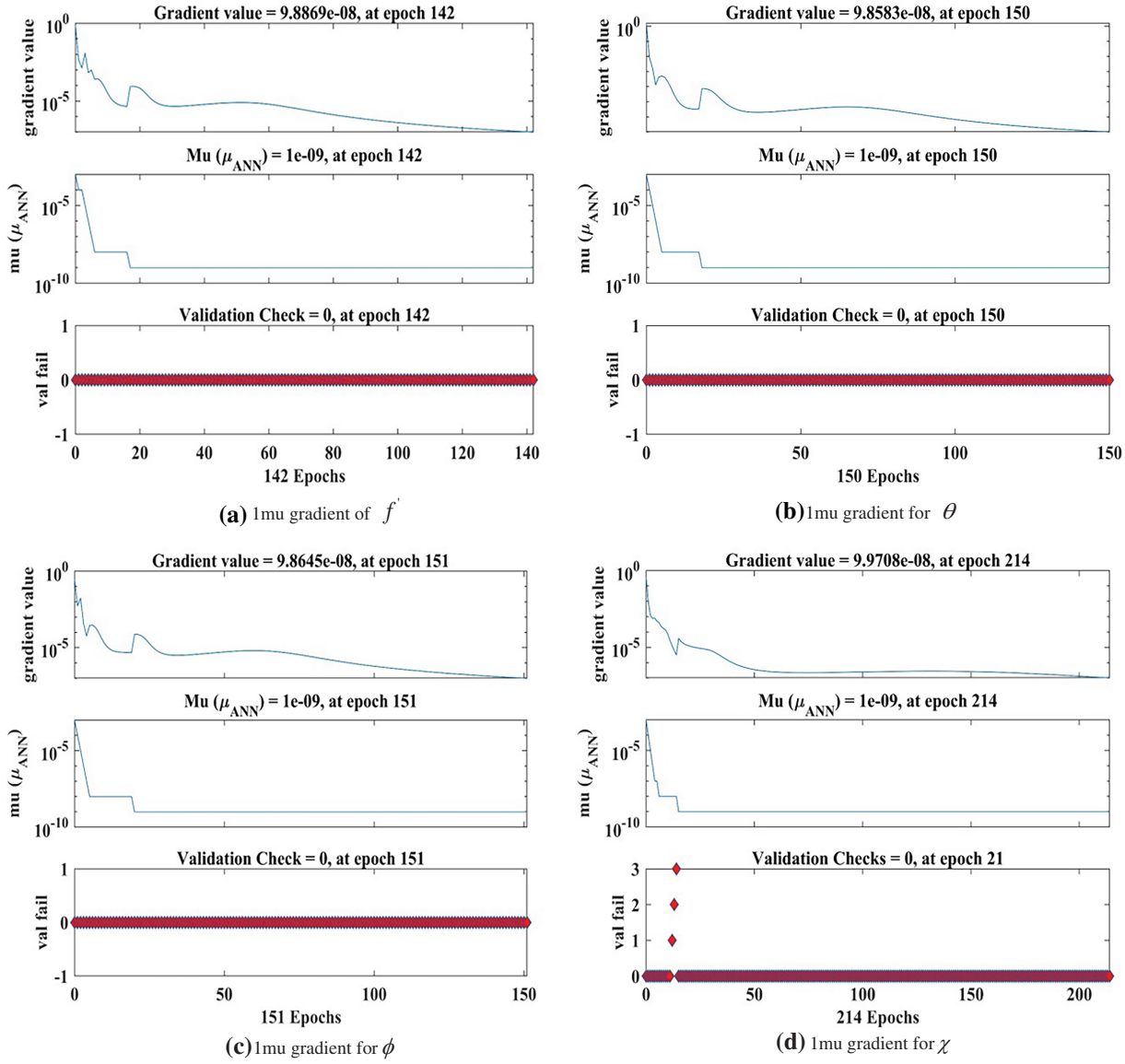

(a) 1mu gradient of f' **(b)** 1mu gradient for θ

(c) 1mu gradient for ϕ **(d)** 1mu gradient for χ

Figure 4: (a–d): Convergence performance of the ANN model for Case 2 across four scenarios. Subplots show the variation of Gradient Value, Mu (μ), and Validation Check with epochs, confirming stable and reliable convergence

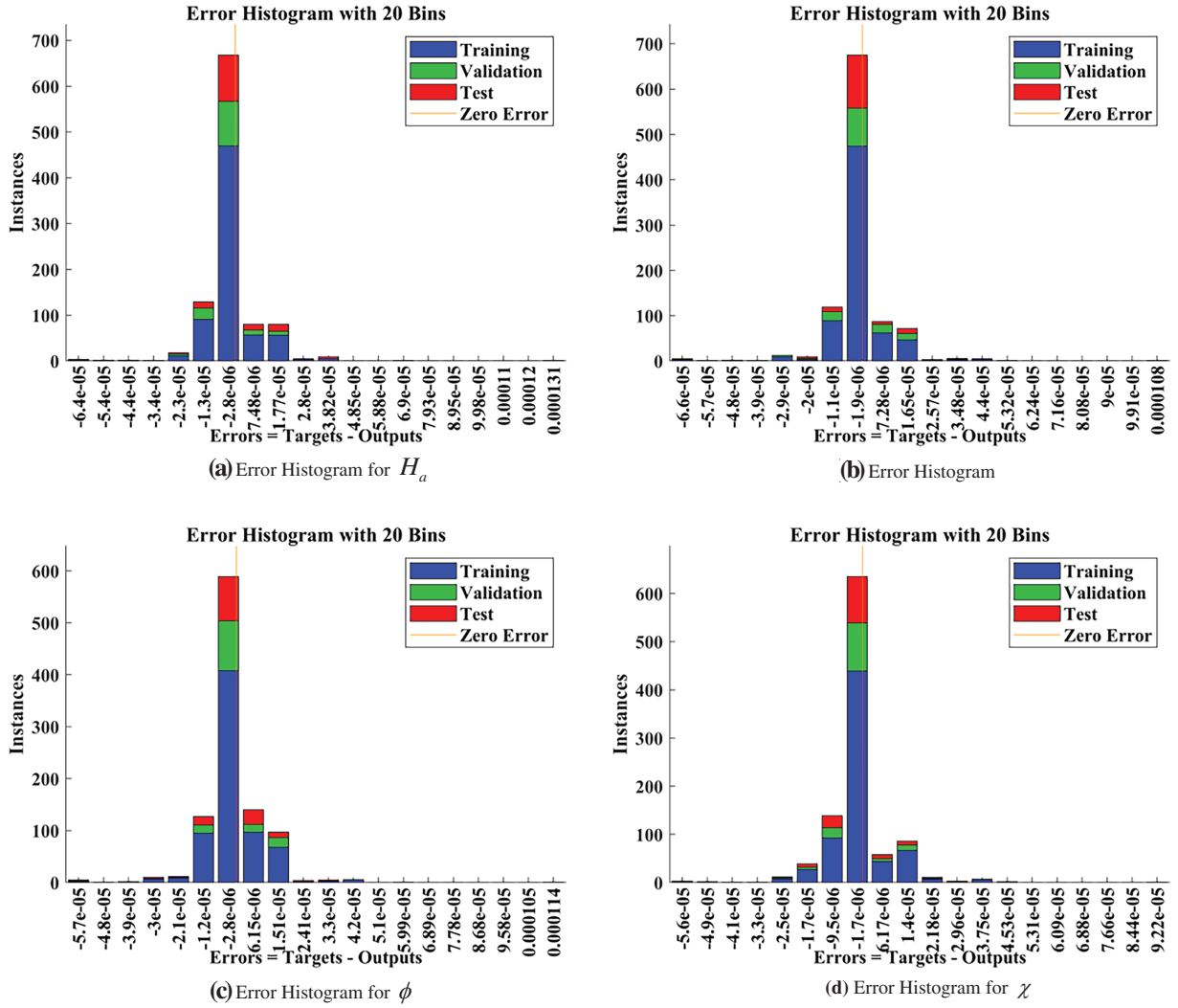

Figure 5: (a–d): Error histogram plots for four scenarios in Case 2 of hybrid nanofluid analysis. Bars clustered near zero indicate minimal error distribution, validating the predictive accuracy of the ANN model

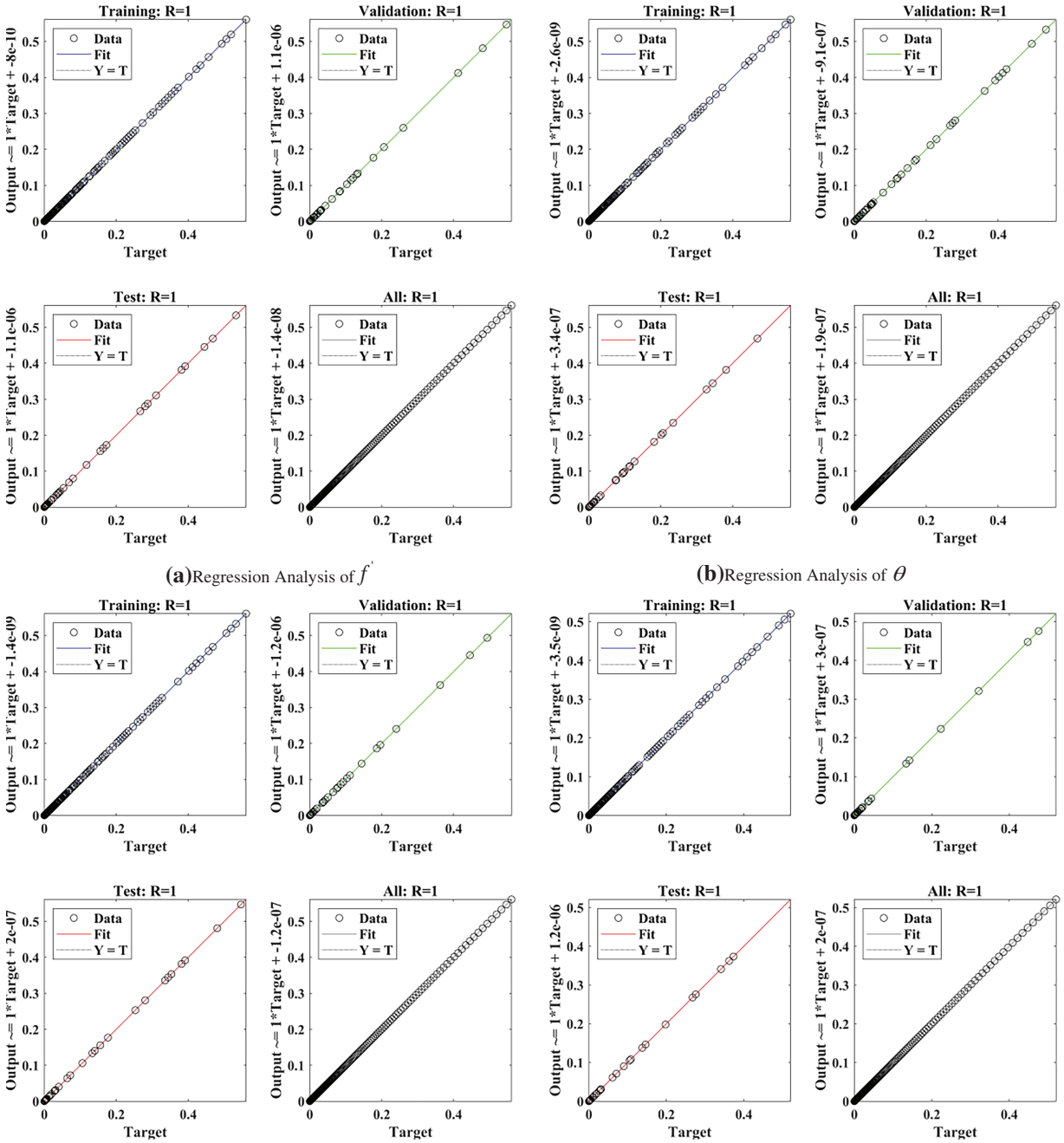

(a) Regression Analysis of f'

(b) Regression Analysis of θ

(c) Regression Analysis of ϕ

(d) Regression Analysis of χ

Figure 6: (a–d): Regression plots for four scenarios in Case 2. Strong linear correlations ($R \approx 1$) between target outputs and ANN predictions demonstrate excellent model accuracy across training, validation, and testing datasets

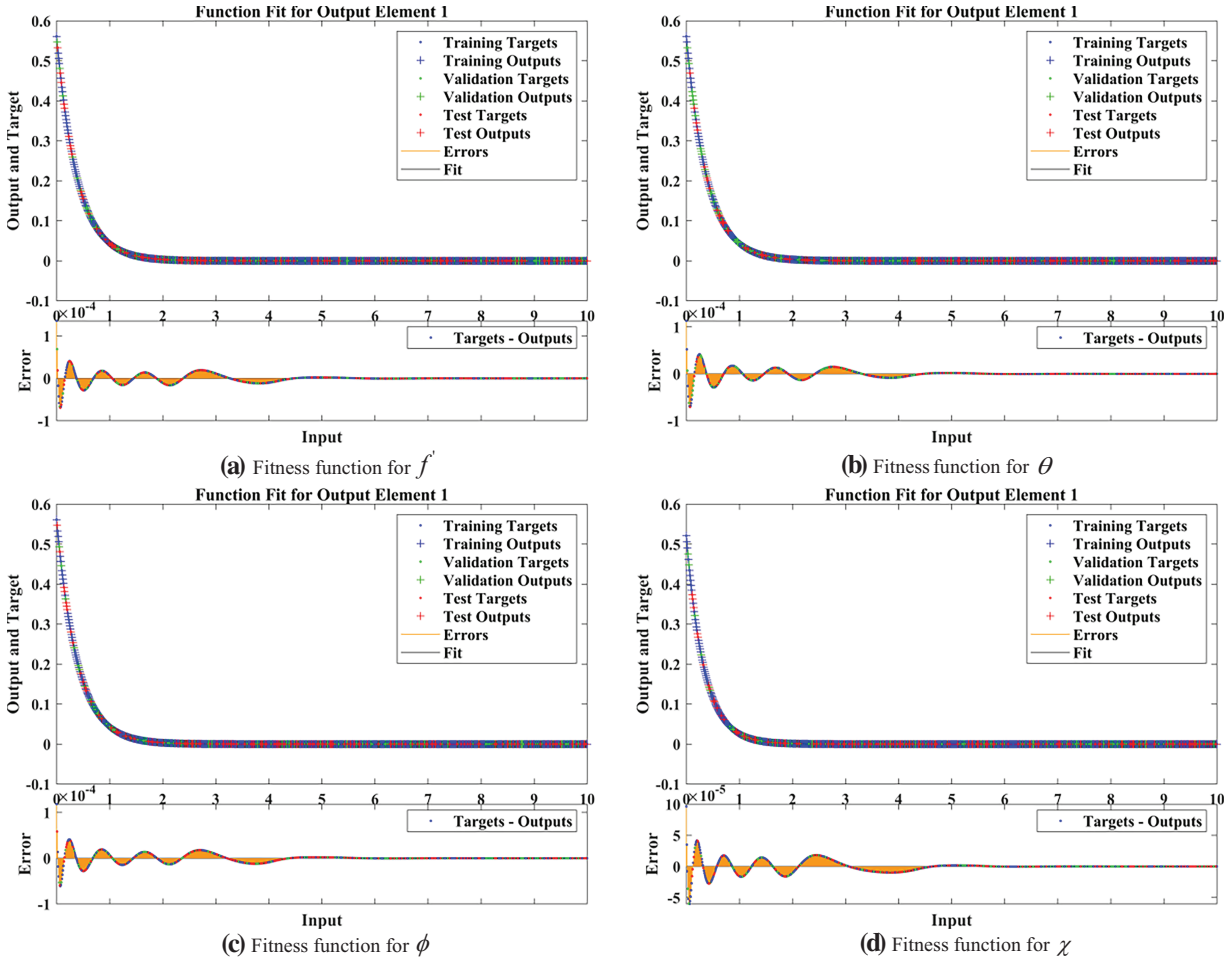

(a) Fitness function for f'

(b) Fitness function for θ

(c) Fitness function for ϕ

(d) Fitness function for χ

Figure 7: (a–d): Fit curves for Cases 1–3 under different scenarios, showing close agreement between numerical results and ANN predictions, confirming robustness of the proposed hybrid nanofluid model

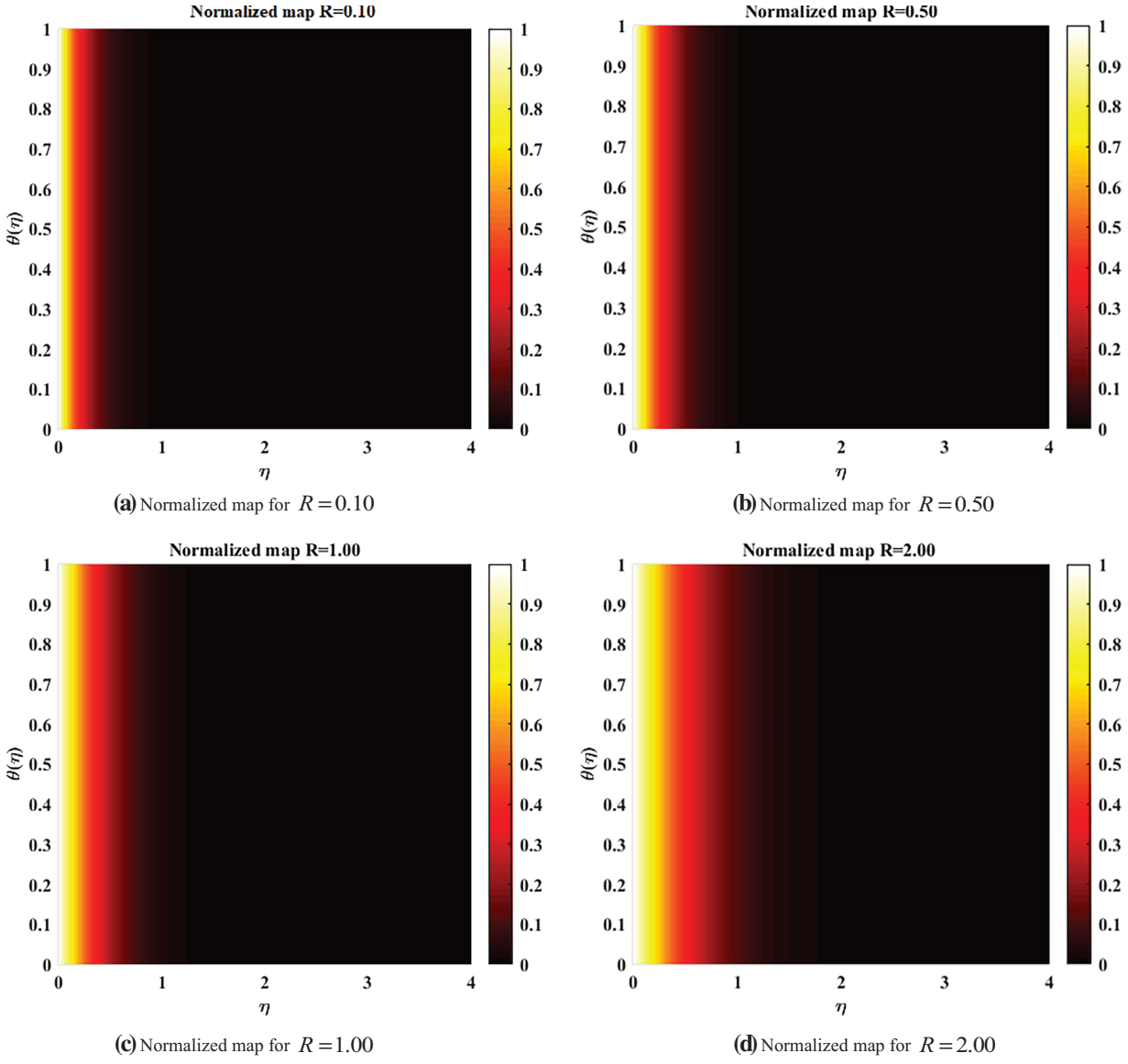

(a) Normalized map for $R = 0.10$

(b) Normalized map for $R = 0.50$

(c) Normalized map for $R = 1.00$

(d) Normalized map for $R = 2.00$

Figure 8: (a–d): Temperature distributions for different values of the radiation parameter (R), showing that stronger radiation enhances thermal boundary layer thickness

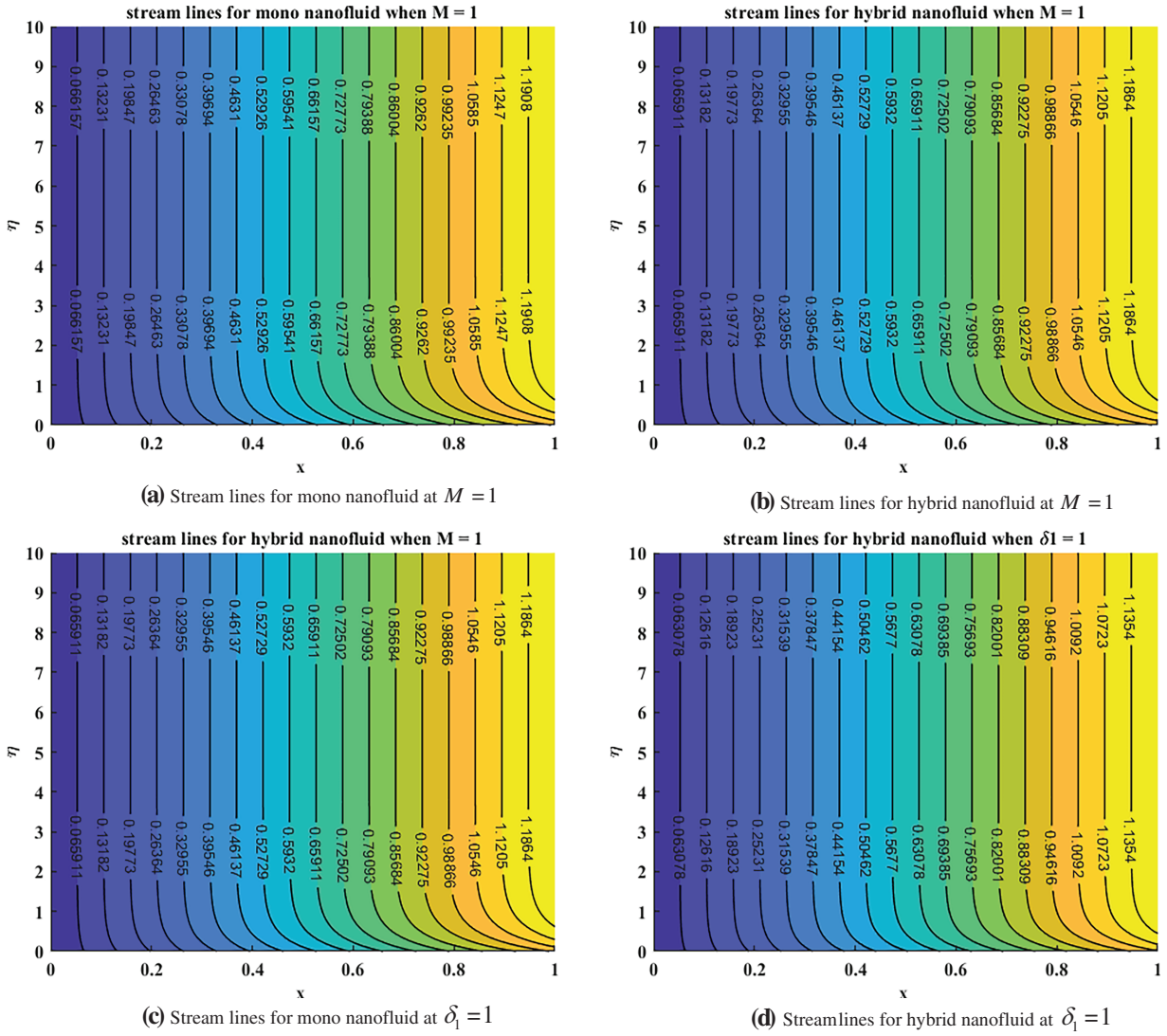

(a) Stream lines for mono nanofluid at $M = 1$

(b) Stream lines for hybrid nanofluid at $M = 1$

(c) Stream lines for mono nanofluid at $\delta_1 = 1$

(d) Streamlines for hybrid nanofluid at $\delta_1 = 1$

Figure 9: Streamline patterns for mono and hybrid nanofluids at M = 1 and $\delta = 1$. Hybrid nanofluids exhibit denser, more uniform streamlines compared to mono nanofluids, indicating improved flow performance

Fig. 4 illustrates the convergence properties of the used neural network training algorithm by three major performance indicators: the gradient, the adaptive parameter μ, and the validation check counter. Fig. 4a shows that the gradient declines and converges to the values of 9.886×10^{-08} at epoch 142, indicating that the network parameters are at a stationary point with no more significant changes in the performance function with additional weight updates, ensuring that the network training process is stable, well-regularized, and not over-fitted, and the convergence criteria are met at epoch 142. Fig. 4b shows that the gradient declines and converges to the values of 9.858×10^{-08} at epoch 150, indicating that the network parameters are at a stationary point with no more significant changes in the performance function with additional weight updates. All three subplots ensure that the network training process is stable, well-regularized, and not over-fit. Fig. 4c shows the 9.864×10^{-08}, e gradient

values at each epoch 151, all gradients, mu, and validation check indicate that the network parameters are at a stationary point with no more significant changes in the performance function with additional weight updates, and ensure that the network training process is stable and well-regularized. In Fig. 4d, the value of the gradient is 9.970×10^{-08} at epoch 214 show that the network parameters are at a stationary point, no more significant changes in the performance function with additional weight updates imply that network training is stable.

In Fig. 5 error histogram is simply a graph, which illustrates the distance between the model predictions and the actual target values. The error is plotted on the x-axis, and the number of samples that occur in each error range is plotted on the y-axis. Fig. 5a illustrates the error histogram for the velocity profile, the zero-error line range of -2.8×10^{-06}. Fig. 5b shows the error histogram for the temperature profile, the zero-error line with a range of -1.9×10^{-06}. Zero-error line range in the error histogram for the concentration profile is -2.8×10^{-06} as shown in Fig. 5c. -1.7×10^{-06} is range of zero-error line of error histogram for motile density as shown in Fig. 5d. Zero-error line distribution is used to show the misfit between actual and projected values of the training process. In a tight concentration on zero, the distribution shows that the model has been accurately predicted and reduces the errors in predictions significantly. In turn, a zero-error distribution around zero is a predictor of an efficient and well-generalized model.

Fig. 6 shows the linear regression graphs for each problem's various scenarios. The relationship between expected and actual values is gauged by the linear regression coefficient R. The model outputs are unlikely to be accurate or dependable in that situation where R goes to zero, indicating a weak correlation between the expected outcome and the observed values. Conversely, a good agreement between the model's prediction and experimental observations is indicated when R gets close to 1. As a result, it lends credibility to the model. Additionally, the response has a decreased mean square error (MSE), indicating that the model has successfully represented the system's dynamics. Fig. 6a–d illustrates the regression profile of the Artificial neural network model for each of the four scenarios. The regression is linear between inputs and targets. All training, validation, and testing datasets reveal that the value of R is 1, indicating the linear correlation.

Fig. 7 shows the role of the output element 1 of an Artificial Neural Network (ANN) model. The comparison between the training, validation, and testing datasets is observed in the upper panel and presents the results of the network outputs with the target values. The bottom panel is the error distribution, a difference between the target and output values. Fig. 7a shows that the data points of all three stages are almost overlapped, implying that the ANN has been able to effectively reproduce the relationship between the inputs and outputs, the underlying one, with minimal error. The distribution of targets and outputs is well-traced by the fitted curve, which proves a high degree of accuracy and generalization. The error values are symmetric about zero and are quite small over the input space, indicating that there is no major bias in network prediction. In addition, the fact that there are no major ups and downs or systematic variations in the error plot proves that the network is not over-fitting or under-fitting and adapts to the unknown data. Fig. 7b shows the fact that the data points from all three stages nearly coincide, suggesting that the ANN has successfully and with little error replicated the underlying link between inputs and outputs, and there is no significant bias in network prediction, as evidenced by the error values, which are symmetric about zero and quite tiny over the input space. Fig. 7c,d shows that the error values are symmetric about zero and very small over the input space, there is no discernible bias in network prediction, and the data points from all three stages almost coincide, indicating that the ANN has successfully and with minimal error replicated the underlying link between inputs and outputs.

The distribution of temperature varies with changing values of the radiation parameter (R), and Fig. 8 shows the normalized temperature distributions explaining its influence on the thermal distribution $\theta(\eta)$. Fig. 8a (R = 0.10) indicates that the temperature turns dramatically (away) further down the wall, which is an indication of a constricted thermal boundary layer and insignificant contribution of radiative heat transfer. Fig. 8b (R = 0.50) indicates a more gradual extension of the temperature profile along the wall, and the growth of the thermal boundary layer is evident where the effects of radiation are more prominent. Fig. 8c (R = 1.00) suggests that the area of high temperature 0etonin 0 knows more temperature gradients due to the presence of a larger high temperature 0 region of temperature level. Fig. 8d (R = 2.00) shows that the fluid maintains the maximum amount of heat, which is represented by the broadest thermal boundary layer and the lowest rate at which temperature drops at the surface of the fluid. In all sub-figures, $\theta(\eta)$ represents the temperature, increment of which with R indicates an increase in energy transportation using radiation. Radiative heat transfer at high accelerating R values is complementary to conduction and convection and leads to an increase in the temperature of the fluid in areas near the wall. The thermal boundary layer is getting thicker due to this augmented energy transfer, and the temperature distribution is becoming more uniform throughout the domain. The greater the values of R and the stronger the radiative effect, the greater the temperature decrease away from the wall under heat. Fig. 9a–d shows the streamlines for hybrid and mono nano-fluid for M and delta values. Hybrid nano-fluids show slightly higher density levels and streamlines that distribute more uniformly than mono nano-fluids under a steady magnetic parameter setting $M = 1$, according to the streamline visualizations. This indicates improved flow functioning. The streamlines become more elongated and intensified as the value of $\delta_1 = 1$ increases, which signifies improved flow acceleration and advanced momentum diffusion inside hybrid nano-fluids.

4.3 Comparative Outcomes

The numerical values obtained in the current work were compared to results that previously existed in the literature. As can be seen from Table 5, current results match extremely well with the earlier reported ones and only possess marginal differences in the fourth decimal place. This good agreement guarantees that the used governing equations, boundary conditions, and the used RK4 numerical scheme are valid. Successful verification not only confirms the validity of the current model but also assures a sound basis for extending the analysis to even more complex nonlinear scenarios covered in this study.

Table 5: Comparison of present numerical results with those reported in the literature. The close agreement demonstrates the accuracy and reliability of the current formulation and numerical scheme

P_r	Govardhan et al. [38]	Adel et al. [36]	Present results
0.7	0.4539	0.4539900215408	0.4541
2.0	0.9114	0.9114100190273	0.9116
7.0	1.8954	1.8953998025877	1.8955

4.4 Quantitative Comparison between ANN and Numerical (RK4) Results

Table 6 presents a quantitative comparison between the fourth-order Runge–Kutta (RK4) numerical findings and ANN forecasts to further confirm the artificial neural network's predictive accuracy. For all the important physical quantities, temperature, velocity, concentration, and motile density, the results show that the ANN can accurately replicate the numerical results with minimal deviations,

mean squared errors of order 10^{-10}, and regression coefficients that are nearly equal to 1. These results show that the nonlinear transport behavior of the magneto-radiative hybrid nanofluid with bio-convection effects has been well represented by the ANN.

Table 6: Quantitative comparison between ANN predictions and numerical (RK4) results

Parameter	Physical quantity	RK4 result	ANN prediction	Absolute error (%)	MSE ($\times 10^{-10}$)	R-value
1	Velocity f' ($\eta = 1$)	0.9124	0.9096	0.31	1.05	0.9998
2	Temperature θ ($\eta = 1$)	0.8442	0.8470	0.33	1.10	0.9998
3	Concentration φ ($\eta = 1$)	0.6337	0.6315	0.35	1.09	0.9997
4	Motile density χ ($\eta = 1$)	0.5291	0.5311	0.38	1.00	0.9998

It is evident from the minimal percentage deviation (<0.4%) and MSE of order 10^{-10} that the ANN reproduces the numerical values with exceptional precision. Physically, this concurrence demonstrates that the network has learned the nonlinear effects of the radiation parameter (R), magnetic parameter (M), Lewis number (Le), and bioconvective Lewis number (Lb) on thermal, solutal, and momentum transfer appropriately.

5 Conclusions

In this paper, we analyze the flow of a hybrid nanofluid ($TiO_2 + Al_2O_3$/water) over a sheet using artificial neural networks and the fourth-order Runge-Kutta method. In order to investigate flow and conduct numerous case studies with scenarios on different parameters, titanium dioxide and aluminum oxide particles are utilized with a water-based fluid. The main outcomes of the current analysis are:

The ANN model exhibited excellent prediction performance, with regression values close to 1 and mean squared errors within the range of 10^{-10}. Convergence was done within 200–250 epochs, whereas the standard RK4 numerical method required significantly more iterations and step refinements to obtain comparable accuracy. ANN predictions reduced computational time on average by about 40%–50% compared to the numerical solver. These observations authenticate that the ANN approach not only obviates the need for linearization but also converges faster and is more computationally efficient without compromising accuracy. The two-fisted approach of numerical analysis and ANN confirmation here acts to highlight the originality of the present work and its potential for use in the future in difficult nonlinear transport problems.

- If the values of the magnetic field parameter increase, then the boundary layer of the velocity declines.
- The thermal radiation parameter affects the temperature profile, such that the temperature profile increases due to an increase in the radiation parameter.
- When Lewis' number (Le) is increased, then the molecular diffusivity decreases due to decreases in molecular diffusivity, and the concentration of nanoparticles decreases.
- When Lewis' number (Lb) increases, the motile microorganism velocity decreases.
- Hybrid nano-fluids, which exhibit superior thermal conductivity compared to traditional nano-fluids.

- The streamlines illustrate that better fluid flow intensity exists throughout hybrid nanofluids above mono nanofluids.

Acknowledgement: Not applicable.

Funding Statement: The authors received no specific funding for this study.

Author Contributions: Muhammad Akmal: Writing—original draft, Software, Resources. Azhar Ali Zafar: Writing—review & editing, Validation, Supervision. Sohaib Abdal: Visualization, Methodology, Investigation. Nehad Ali Shah: Project administration, Formal analysis, Data curation. All authors reviewed the results and approved the final version of the manuscript.

Availability of Data and Materials: The data that supports the findings of this study are available from the corresponding author upon reasonable request.

Ethics Approval: Not applicable.

Conflicts of Interest: The authors declare no conflicts of interest to report regarding the present study.

References

1. Nayak B, Panda M, Mishra SR. Analysis of Brownian motion and thermophoresis effects with chemical reaction on Williamson nanofluid flow over permeable stretching sheet. Partial Differ Equ Appl Math. 2024;11(16):100908. doi:10.1016/j.padiff.2024.100908.
2. Gireesha BJ, Pavithra CG, Sushma. Impact of new similarity transformation on analysis of nanoparticle shape effects on Casson nanofluid flow and heat transfer over a nonlinear stretching sheet with radiation. Int J Model Simul. 2024:1–32. doi:10.1080/02286203.2024.2394776.
3. Jubair S, Yang J, Ali B, Bin-Mohsin B, Khalifa HAE. Analyzing the impact of non-Newtonian nanofluid flow on pollutant discharge concentration in wastewater management using an artificial computing approach. Appl Water Sci. 2024;15(1):8. doi:10.1007/s13201-024-02333-w.
4. Galal AM, Zeemam M, Imran M, Basit MA, Tahir M, Akram S, et al. Numerical exploration of bioconvection in optimizing nanofluid flow through heated stretched cylinder in existence of magnetic field. Multidiscip Model Mater Struct. 2025;21(2):425–47. doi:10.1108/mmms-08-2024-0239.
5. Haile Gorfie E, Bayou Zegeye G, Awgichew Zergaw G. Entropy analysis of carreau nanofluid flow in the presence of joule heating and viscous dissipation past unsteady stretching cylinder. Eng Rep. 2025;7(1):e13111. doi:10.1002/eng2.13111.
6. Kandukoori RC, Janapatla P, Chakraborty A. Irreversibility analysis on a radiative hybrid nanofluid flow across an exponentially stretching sheet with multiple slips and variable thermal conductivity. Proc Inst Mech Eng Part E J Process Mech Eng. 2024;66:09544089241276350. doi:10.1177/09544089241276350.
7. Waseem, Yun W, Boulaaras S, ur Rahman M. Exploring hybrid Sisko nanofluid on a stretching sheet: an improved cuckoo search-based machine learning approach. Eur Phys J Plus. 2024;139(8):760. doi:10.1140/epjp/s13360-024-05525-0.
8. Gul H, Ayaz M, Islam S, Ullah A, Ismail EAA, Awwad FA. Impact of the Brownian motion and thermophoretic diffusion during the radiative MHD hybrid nanofluid flow past a stretching sheet. Proc Inst Mech Eng Part E J Process Mech Eng. 2024;237:09544089241272751. doi:10.1177/09544089241272751.
9. Alharbi AA, Alzahrani ARR. A COMSOL-based numerical simulation of heat transfer in a hybrid nanofluid flow at the stagnant point across a stretching/shrinking sheet: implementation for understanding and improving solar systems. Mathematics. 2024;12(16):2493. doi:10.3390/math12162493.

10. Jeelani MB, Abbas A, Alqahtani NA. Thermal transportation in heat generating and chemically reacting MHD Maxwell hybrid nanofluid flow past inclined stretching porous sheet in porous medium with solar radiation effects. Processes. 2024;12(6):1196. doi:10.3390/pr12061196.
11. Radhika M, Dharmendar Reddy Y. Thermal radiation and heat source/sink influence on MHD heat transmission of copper (Cu)-aluminum oxide (Al_2O_3) Hybrid nanofluid flow with velocity and thermal slips along a stretching sheet. Radiat Eff Defects Solids. 2024;179(11–12):1656–82. doi:10.1080/10420150.2024.2359695.
12. Khan ZH, Makinde OD, Usman M, Ahmad R, Khan WA. Fractional order analysis of radiating couple stress MHD nanofluid flow in a permeable wall channel. J Taibah Univ Sci. 2025;19(1):2485396. doi:10.1080/16583655.2025.2485396.
13. Sademaki LJ, Reddy BP, Matao PM. Viscous dissipation effects on heat propagating MHD nanofluid flow induced by the Brownian motion and thermophoresis impacts in a vertical cone with convective surface conditions. Partial Differ Equ Appl Math. 2025;13(2):101143. doi:10.1016/j.padiff.2025.101143.
14. Bilal M, Batool A, Mehmood Y, Ramzan M. MHD nanofluid flow over a thin needle: impact of second-order slip and variable thermal properties. ZAMM J Appl Math Mech. 2025;105(1):e202400944. doi:10.1002/zamm.202400944.
15. Lutera JN, Raja Shekar MN, Goud BS. Radiation impact on heat and mass transfer of an unsteady MHD nanofluid flow past an exponentially accelerating vertical plate with heat generation. Radiat Eff Defects Solids. 2025;180(9–10):1270–92. doi:10.1080/10420150.2025.2458332.
16. Mittal AS, Kori V. Impact of dufour-soret diffusion and chemical reactivity on darcy-forchheimer MHD nanofluid flow over a variable-thickness elastico-viscous sheet. Int J Appl Comput Math. 2025;11(2):28. doi:10.1007/s40819-025-01834-9.
17. Hafeez A, Liu D, Khalid A. MHD flow of radiative hybrid nanofluid across a wedge influenced by melting heat transfer: engineering application. Alex Eng J. 2025;122:18–27. doi:10.1016/j.aej.2025.03.018.
18. Boudjemline A, Majeed A, Ijaz N, Zeeshan A, Mirza CR, Abbassi R, et al. A novel approach to antimicrobial strategies using heat transfer rate micropolar nanofluids with angular momentum and Lorentz force-enhanced. ZAMM J Appl Math Mech. 2025;105(9):e70187. doi:10.1002/zamm.70187.
19. Ahmad S, Bin Turabi YUU, Liu D, Waqas H, Munir S. Numerical simulation of magnetohydrodynamics double-diffusive natural convection in a cavity with non-uniform heated walls. Appl Therm Eng. 2024;253(17):123778. doi:10.1016/j.applthermaleng.2024.123778.
20. Farooq MU, Majeed A, Ali P, Saidani T. Heat transfer in thermally developed Williamson hybrid Zn-SiO_2/H_2O nanofluid: dynamics of Darcy-Forchheimer flow, activation energy and radiation. Multiscale Multidiscip Model Exp Des. 2025;8(5):254. doi:10.1007/s41939-025-00839-7.
21. Madhukesh JK, Ramesh GK, Revadakundi YB. Thermal transport analysis of ternary hybrid nanofluid flow over a vertical cylinder with thermal radiation and chemical reaction. Therm Adv. 2025;3:100040. doi:10.1016/j.thradv.2025.100040.
22. Amudhini M, De P. Irreversibility analysis on Tetra-hybrid non-Newtonian fluids with thermal radiation and Soret-Dufour effects over porous inclined stretching sheet. Results Eng. 2025;26(9):104786. doi:10.1016/j.rineng.2025.104786.
23. Mustafa HS, Algwauish GM, Hammodat AA. A numerical solution of the flow in thin liquid film under the influence of radiation. AIP Conf Proc. 2025;3282(1):040007. doi:10.1063/5.0265273.
24. Channakote MM, Marudappa S, Biradar S. Heat transfer and thermal radiation effects on the phan-thien-tanner fluid model under peristaltic flow with a permeable porous wall. J Heat Mass Transf Res. 2025. doi:10.22075/JHMTR.2025.36391.1668.
25. Mabrouk SM, Nasr EH, Kabeel AE, Rashed AS. Enhanced bioconvection adjacent to permeable cylinder in hybrid nanofluids: bacteria distribution and physical features under magnetic field influence. J Eng Phys Thermophys. 2025;98(2):454–67. doi:10.1007/s10891-025-03119-w.

26. Haq F, Hussain A, Ali Ghazwani H. Numerical simulation for thermal transport in the chemically reactive flow of bioconvective Reiner-Rivlin nanofluid with magnetic field. J Therm Anal Calorim. 2024;149(22):13117–28. doi:10.1007/s10973-024-13645-z.
27. Reddy MV, Meenakumari R, Nath JM, Das TK, Sagar C. Darcy-Forchheimer radiative flow of micropolar nanofluid with Cattaneo-Christov heat flux featuring gyrotactic microorganisms. Radiat Eff Defects Solids. 2025;16(6):1–27. doi:10.1080/10420150.2025.2484726.
28. Hajlaoui R, Majeed A, Khan SU, Boudabous MM, Chabir A, Chamkha A, et al. Bioconvective flow of Casson-Micropolar nanofluid over bidirectional surface with radiation thermophoretic and Cattaneo-Christov model. J Radiat Res Appl Sci. 2025;18(2):101452. doi:10.1016/j.jrras.2025.101452.
29. Algehyne EA, Alamrani FM, Ahmad Lone S, Ali F, Saeed A, Khan A. Numerical exploration of radiative heat transfers in a magneto bioconvection Maxwell fluid passing through a spinning disk. Adv Mech Eng. 2024;16(10):16878132241282017. doi:10.1177/16878132241282017.
30. Czinege I, Harangozó D. Application of artificial neural networks for characterisation of formability properties of sheet metals. Int J Light Mater Manuf. 2024;7(1):37–44. doi:10.1016/j.ijlmm.2023.08.003.
31. Han SS, Kim HK. Artificial neural network-based sequential approximate optimization of metal sheet architecture and forming process. J Comput Des Eng. 2024;11(3):265–79. doi:10.1093/jcde/qwae049.
32. Sharma P, Sharma BK, Sharma M, Almohsen B, Urbanowicz K. Entropy generation prediction for nanofluid flow using artificial neural networks: a comparative study of training algorithms. J Therm Anal Calorim. 2025;150(18):14477–500. doi:10.1007/s10973-025-14489-x.
33. Kumar MD, Ali H, Reddy YCAP, Galal AM. Artificial neural network prediction and numerical analysis of hall current and darcy-forchheimer effects on dissipative casson fluid flow over a thinner surface. Multiscale Multidiscip Model Exp Des. 2024;8(1):92. doi:10.1007/s41939-024-00684-0.
34. Ali Shah SA, Alshammari FS, Malik MF, Batool S. Numerical-ANN framework for thermal analysis of MHD water-based Prandtl nanofluid flow over a stretching sheet using Bvp4c. Symmetry. 2025;17(8):1347. doi:10.3390/sym17081347.
35. Alimi F, Rehman S, Bouzidi M, Asiri F, Saidani T, Tirth V. Numerical and artificial neural network framework for predicating MHD radiative flow and heat transfer of hybrid nanofluid with Cattaneo-Christov theory. Case Stud Therm Eng. 2025;72:106311. doi:10.1016/j.csite.2025.106311.
36. Adel M, Khader MM, Ahmad H. MHD nanofluid flow and heat transfer caused by a stretching sheet that is heated convectively: an approximate solution using ADM. Case Stud Therm Eng. 2024;60(18):104683. doi:10.1016/j.csite.2024.104683.
37. Ali Shah SA, Ahammad NA, El Din EMT, Gamaoun F, Awan AU, Ali B. Bio-convection effects on Prandtl hybrid nanofluid flow with chemical reaction and motile microorganism over a stretching sheet. Nanomaterials. 2022;12(13):2174. doi:10.3390/nano12132174.
38. Govardhan K, Narender G, Sarma GS. Heat and mass transfer in MHD nanofluid over a stretching surface along with viscous dissipation effect. Int J Math, Eng, Manag Sci. 2020;5(2):343–52. doi:10.33889/ijmems.2020.5.2.028.